Towards a Self-Powered Structural Health Monitoring Smart Tire

Howard J. Chung

Thesis submitted to the Faculty of the
Virginia Polytechnic Institute and State University
in partial fulfillment of the requirements for the degree of

Master of Science
in
Aerospace Engineering

Michael K. Philen , Co-Chair
Pablo A. Tarazaga, Co-Chair
Andrew J. Kurdila

May 2, 2016
Blacksburg, Virginia

Keywords: Piezoelectric, Impedance-Based Structural Health Monitoring, Energy Harvesting, Zinc Oxide Nanowires, Smart Tires, Smart Materials

Towards a Self-Powered Structural Health Monitoring Smart Tire

Howard J. Chung

TECHNICAL ABSTRACT

This work investigates the feasibility of developing a self-powered structural health monitoring (SHM) smart tire using piezoelectric materials. While this work is divided into two components: SHM and energy harvesting, the context of smart tire in this work is defined as the development of a SHM system that (i) has self-powering capabilities, and (ii) addresses the potential of embedding sensors. The use of impedance based SHM on a tire is severely limited due to the low stiffness and high damping characteristics of the tire. This work propose the use of a high voltage impedance analyzer, and the addition of electrical circuit to enhance the damage detection process. Experimental work was conducted on an aluminum beam and on a tire section with commercially available piezoelectric sensors. The use of a high voltage impedance analyzer was demonstrated to provide insight on damage type and damage location. Two sensors were connected in parallel as an effective sensory system, and was shown to reduce interrogation time, but reduce damage identification sensitivity. With added electrical circuits, a belt separation on the tire was successfully detected by the shift in electrical impedance signature. For the energy harvesting portion of this work, a bimorph piezoelectric energy harvester model was derived using extended Hamilton's principle and the linear constitutive relations of piezoelectric materials. Comparison of model with experimental data at increasing loading conditions demonstrated the monotonic increase in voltage output, with linear asymptotes at extreme loading conditions (short-circuit and open-circuit). It also demonstrated the existence of an optimal resistive load for maximum power output. To address the ability to embed sensors, an existing fabrication process to grow arrays of ZnO nanowires in carbon fiber reinforced polymer was used in this work. Comparison of power generation from a composite beam with ZnO nanowires with a composite beam without ZnO nanowires demonstrated the power generation capabilities of the nanowires. A maximum peak voltage of 8.91 mV and peak power of 33.3 pW was obtained. After the application of 10V DC, a maximum of 45 pW was obtained. However, subsequent application of 20V DC reduced the maximum peak power output to 2.5 pW. Several attempts to increase power generation including adding a tip mass and changing the geometry of the composite beam were conducted. Finally, the theoretical voltage frequency response function obtained from the theoretical piezoelectric constant and dielectric constant of a single ZnO nanowire were compared to the experimental voltage frequency response function. The discrepancies were discussed.

Towards a Self-Powered Structural Health Monitoring Smart Tire

Howard J. Chung

GENERAL AUDIENCE ABSTRACT

Currently, in-service automobile tires operate on the principle of safe life and are monitored by visual inspection. However, tire damages such as thread damages, cuts, and broken beads are distinctive for each individual based on driving conditions, usage frequencies, and maintenance quality. These unwanted damages could lead to tire failures causing loss of properties and loss of life. The need to provide in-service state awareness of a tire's structural integrity triggered the research of "Intelligent Tires" or "Smart Tires". Within the last three decades, extensive research has been conducted to integrate piezoelectric materials on aerospace, civil, and mechanical engineering infrastructure for the use of structural health monitoring (SHM) and energy harvesting. This is due to the unique electro-mechanical properties and multifunctional capabilities of the material. The direct effect of piezoelectric material is that it produces electrical charge under application of mechanical stress. Likewise, its converse effect is that it produces mechanical strain under application of electrical field. Using such unique material properties, this research seeks to integrate such material onto automobile to investigate the feasibility of developing a self-powered SHM smart tire. This research is thus divided into two components: SHM, and energy harvesting. For the first component, experimental testing was conducted on using a technique termed impedance-based SHM on an aluminum beam and on a tire section. Limitations of the technique were discussed, and proposals to enhance damage identification sensitivities were explored. For the second component, theoretical prediction and experimental testing was conducted. A unique nano-scale piezoelectric material called ZnO nanowires was opted for this study for ease of embedding the sensors in the future. Maximum voltage and power generation by these ZnO nanowires were characterized. The implementation of such smart tire creates the potential to improve road safety and to transition from schedule-based maintenance to condition-based maintenance. Using advanced diagnosis and prognosis techniques, operators can inspect and repair tires less often, and reduce the risk of failures, thus reduce cost. With the energy harvesting element included, the needs to replace batteries, or to install wires for energy supply are eliminated, making the system easy to use with minimal maintenance effort.

Acknowledgments

I would like to thank my co-advisors Dr. Michael Philen and Dr. Pablo Tarazaga for offering the support and guidance in helping me complete my thesis. It is an absolute pleasure to work with two leading experts in the field of aerospace engineering and mechanical engineering. On top of providing the financial support to make this work successful, both advisors have provided for me strong mentorship and comradery within their research groups. I also want to thank Dr. Andrew Kurdila for teaching me the fundamentals of piezoelectricity, and guiding me towards the right resources, without which, I will be unable to appreciate the applied work conducted in this research experience.

I want to thank my parents, Lawrence and Ellie Chung for providing unequivocal support and encouragement for me to complete my thesis. Their wise and comforting words given during difficult times throughout this work are truly appreciated.

It is truly a unique thesis where I was placed in a position to contribute in two different research work, but with similar research theme. On the SHM work, I want to thank Sriram Malladi, and Mohammad Albakri, for helping me get up to speed with the state-of-the-art of impedance-based SHM. I want to thank everyone in the Vibrations, Adaptive Structures, and Testing Laboratory for their friendship in this journey. I also want to thank Ron Kennedy and Meysam Khaleghian for addressing my questions on the mechanics of tires and providing best practices advice.

I want to thank my lab partners at the Aerospace Structures and Materials Laboratory, Lori Groo, Sean Offenberger, Julian Brown, Engin Sengezer and Brady Doepke for assisting me in the energy harvesting work. I also want to thank Ayoub Boroujeni, Anahita Emami, and Dr. Marwan Al-Haik for fabricating the ZnO nanowire samples.

Lastly, I want to thank my office-mate Cao Shun Xiang for his often witty remarks made in this journey. He has provided companionship during long-hours in the office, but in particular during times of discouragement have encouraged me and others with his favorite Chinese proverb, which translates figuratively to ”Do not worry, everything will turn out for the best”.

Contents

Chapter 1

Introduction

1.1 History and Motivation

In 2000, the U.S. Transportation Recall Enhancement, Accountability, and Documentation (TREAD) legislation have mandated the installation of the Tire Pressure Monitoring System (TPMS) [1]. The TPMS measures tire air pressure and warns vehicle drivers when one or more tires are significantly under-inflated. Under-inflation of tires is one of the many causes creating unsafe driving conditions, and may lead to disastrous tire failures such as tire separation and tire blowouts [2]. These failures arise from various tire damages such as tread damage, bead damage, sidewall damage, separation, and inner-liner abrasion. While TPMS detects the occurrence of tire under-inflation, it could not detect other root causes of tire damages such as high-speed impact, over-deflection, and ozone deterioration. Moreover, tire damages are identified by visual inspection over schedules determined by surveying a fleet of tires [3]. Currently, the state-of-the-art nondestructive testing technique used by automotive tire manufacturers for tire inspection is called shearography. Shearography is a full-field, noncontact, nondestructive inspection technique that uses the principle of interferometry to detect cracks and voids [4]. However, shearography identifies anomalies from manufacturing processes, and is not commonly used to inspect the structural integrity of a tire that has been in-service.

The need to provide in-service state awareness of a tire's structural integrity triggered the research of "Intelligent Tires" or "Smart Tires". A smart tire is a tire equipped with in-situ sensing mechanisms that could be used to monitor pressure, strain, temperature, and is equipped with actuators and control systems that could be used to improve road safety [5–8]. Within the last three decades, extensive research have been conducted on integrating piezoelectric materials on aerospace, civil, and mechanical engineering infrastructure for structural health monitoring (SHM) and energy harvesting applications [9–12]. Piezoelectric materials are keenly suited for such applications due to their electro-mechanical coupling, making them capable of serving as collocated sensors and actuators. SHM is the process of identifying damage and providing in-service state awareness of an infrastructure's structural integrity. The damage identification process can be outlined with identifying the following: (i) existence of damage, (ii) damage location, (iii) types of damage, and (iv) damage severity [12]. Implementing SHM systems on an automobile tire creates the potential to improve road safety, and to transition from schedule-based maintenance (SBM) to condition-based maintenance (CBM). In contrary to SBM, CBM uses these in-situ sensing mechanisms in conjunction with advanced diagnosis and prognosis techniques to guide maintenance practices. This would greatly benefit operators by inspecting and repairing less often, and reducing the risk of failures, thus reducing cost [13].

Previous research demonstrated that after the establishment of the operational evaluation of SHM, one needs to establish an appropriate sensor network to achieve tasks like data acquisition, data transmission, data processing and data storage [10]. Recently, rapid advances in wireless technologies and low-powered electronics have attracted researchers to integrate them into autonomous SHM systems [14]. The most attractive element of such systems is the elimination of external cable access to traditional power sources [10]. In an effort to make sensing networks truly autonomous, research was conducted to eliminate the need for battery changes while conducting SHM [10, 15, 16]. Although various strategies for harvesting, or scavenging energy from the environment have been studied, including large-scale alternative energy generations like wind turbines and solar cells, conversion of mechanical energy to electrical energy using piezoelectric materials remain one of the most promising solutions for small, low-power, embedded sensing system [10, 17–19].

1.2 Current Solutions

1.2.1 Structural Health Monitoring

Advanced smart tires that measure parameters other than pressure can be categorized into indirect tire monitoring and direct tire monitoring [6]. Most advanced indirect tire monitoring uses measured parameters such as velocity, wheel angular speed, and normal forces applied to the tires to determine tire-road friction coefficient and infer driving conditions like dry road, wet road, snowy road, or icy road [6, 20]. Lee developed a real-time maximum tire-road friction coefficient estimator that could be used to adjust the vehicle to a safe velocity [20]. Yi proposed using wheel slip, vehicle velocity, and normal load on the tire to estimate tire-road characteristics that is used to control emergency braking maneuvers [21]. However, these methods often require complex algorithms to estimate tire-road conditions [6, 22, 23]. Also, while knowledge of tire-road conditions are used to enhance other active control safety systems, it does not provide any information on the structural integrity of the tire itself.

Advanced direct tire monitoring, on the other hand, directly measures tire deformation. Palmer suggested the use of fiber optic microelectromechanical systems (MEMS) that is based on Luna's patented extrinsic Fabry-Perot interferometer (EFPI) to measure strain [13]. Pohl proposed the use of surface acoustic wave sensors for the measurement of friction between tires and road surface [24]. Yi used a piezoelectric polyvinylidenefluoride (PVDF) based sensor embedded inside a skid-steered mobile robot to correlate thread deformation and ground conditions such as wheel slip and friction coefficient. Gondal used a new sensing material called Metal Rubber$^{\mathrm{TM}}$ which exhibits the conductivity of metals, and the flexibility of rubber to measure localized strain. Most of these sensing techniques require the bonding of sensors on the surface of the inner liner of the tire. However, previous research has shown that the large difference between the stiffness of externally bonded sensors and that of rubber contributes to sensor de-bonding [6, 8]

In an attempt to reduce the difference in stiffness between sensors and tire, Matsuzaki suggested using the capacitance-resistance change between two adjacent steel belts in a tire as a strain sensor [25]. The system was demonstrated on a rectangular specimen cut from a truck tire, on static and dynamic tension tests. Results show that capacitance decreases as the tire specimen was held under tensile load, and that there is almost a near linear relationship between the fundamental frequency of the oscillating circuit and applied strain [25]. Matsuzaki also proposed using a flexible patch-type strain sensor utilizing electric capacitance change. The capacitance of the sensor, which was made from flexible polymide substrates and ultra-flexible epoxy resin, was shown to not exhibit hysteresis, but was shown to increase due to temperature increases [26]. Another patch-type strain sensor that is rubber-based was fabricated using photolithography. This sensor works under the same principle, and was shown to be able to measure strain up to 14% [27]. While reducing the difference in stiffness between externally bonded sensors and the tire material reduces the occurrence of sensor debonding, a more practical solution that needs more research is to embed active smart materials into load-bearing structures.

Previous forms of advanced smart tires, both direct and indirect tire monitoring, provide many insights on usage monitoring, but do not indicate presence of damage nor quantify its severity. Another non-destructive method of indicating damage is the impedance-based SHM technique [28–30]. Impedance-based SHM is a proven way of detecting damage in various applications, including civil structures [31], pipelines [32], and wind turbines [33]. Previous research has shown that the electrical impedance of a piezoelectric sensor is directly related to the mechanical impedance of the host structure, to which the piezoelectric sensor is bonded [28]. Leveraging the coupled electro-mechanical coupling of piezoelectric sensors, one can quantify damages in the structure by measuring the electrical impedance of the sensor.

1.2.2 Energy Harvesting

For mechanical systems, the two most commonly used vibration-based energy harvesters to convert mechanical energy to electrical energy are based on electromagnetic or piezoelectric effects. An electromagnetic transducer constitutes a coil and a permanent magnet tied to a spring, where electricity is generated by the principle of magnetic induction. Many researchers have demonstrated the feasibility of using electromagnetic generators to harvest energy from low-frequency vibrations of bridges to power SHM nodes [34–36]. Glynne-Jones designed a miniature electromagnetic generator that is capable of producing a peak power of 3.9 mW when mounted on the engine block of a car [37]. However, the design of electromagnetic generator is most beneficial when the resonant frequency of the harvester is matched with the frequency of vibrations seen at the structure of interest [38].

Piezoelectric material is an active material that converts mechanical energy into electrical energy without any complex structure. The most common type of piezoelectric energy harvesting is the cantielever type harvester [19, 39]. Theoretical modeling of cantilever type piezoelectric energy harvester has been well studied and documented [19, 39, 40]. Experimentally, Sodano investigated a monolithic piezoelectric, bimorph QuickPack and macro fiber composite energy harvesting devices to determine their capacity to recharge a battery [41]. Shen used a piezoelectric cantilever with a micromachined Si proof mass for low frequency vibration energy harvesting application [42].

Implantable and wearable piezoelectric power supplies have shown promising success in the integration of piezoelectric materials. Kymissis integrated a piezoceramic composite material in the heel of a shoe and a multilayer PVDF foil laminate in the sole of the shoe, and harvested mechanical energy from walking to power a radio transmitter [43]. Mateu showed how to analytically construct an optimum beam-type shoe insert, taking into account the normal walking activity, the force exerted on the insert, and the piezoelectric film properties [44]. Swallow suggested the development of a micropower generator using microcomposite based piezoelectric materials for energy harvesting in glove structures [45]. These works demonstrate the feasibility of integrating piezoelectric energy harvesters into daily used mechanical objects, including tires to power low-power electronics.

More recently, the development of nano-scale energy harvesters, including piezoelectric Zinc Oxide (ZnO) nanowires is attracting significant attention [46–48]. These ZnO nanowires have been grown on different substrates such as GaN/sapphire, glass fiber and flexible cellulose-based paper, and have shown promising energy harvesting capabilities [47, 49, 50]. To make ZnO nanowires adaptable to applications that are elastic or deformable, Masghouni suggested embedding ZnO nanowires in carbon fiber reinforced polymer and demonstrated growing vertically aligned ZnO nanowires array on a plain-woven carbon fiber substrate [51]. Previous work have shown energy harvesting capabilities when ZnO nanowires are grown on Kevlar aramid fabric [52] and on carbon fiber fabric [51], demonstrating the functionality of these nanowires when they are grown on different substrate. To demonstrate its applicability on road safety, Lin fabricated transparent flexible nanogenerators using flexible polydimethlsiloxane (PDMS) substrate for the growth of ZnO nanowires, and used it as a self-powered sensor for monitoring vehicle speed and detecting vehicle weight [53]. Hu bonded a flexible nanogerator using flexible polyester substrate and ZnO nanowire textured films on the inner liner of a bicycle tire and harvested energy when the tire was subjected to compressive load. She demonstrated the increase in power generation when multiple nanogenerators were connected in parallel, and harvested a maximum output power density of 120 $\mu W cm^{-2}$ [46].

1.3 Problem Statement and Research Objectives

Currently, in-service automobile tires operate on the principle of safe life and maintenance by visual inspection. Tire damages such as thread damage, cuts, and broken bead could lead to tire failures causing loss of properties and loss of life. From a tire maintenance perspective, damages such as punctures and cuts are usually visually identifiable. Hence, this work will specifically target the damage type known as separation, as illustrated in Figure 1.1.

Figure 1.1: Types of non-visually identifiable tire damages; Left: Belt separation; Center: Bead separation; Right: Shoulder Separation [54]

Farrar and Worden [12] outlined the process of an autonomous SHM system in four steps shown in Figure 1.2. Under each step are different problems or topics that need to be investigated to achieve a fully autonomous SHM system. Leveraging previous successful efforts in developing smart civil, aerospace, and mechanical structures, this work will address the highlighted problems in Figure 1.2 to develop a self-powered SHM smart tire.

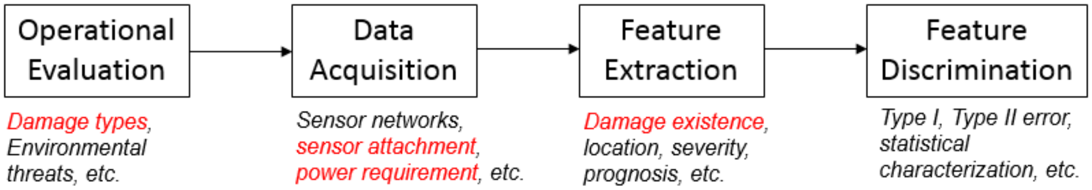

Figure 1.2: Consideration for an ideal autonomous structural health monitoring system

Under each step outlined in Figure 1.2 exists a plethora of research themes that need to be addressed before an autonomous SHM system can be realized. However, a few can be addressed simultaneously due to the multifunctional capability of piezoelectric materials. The problem statement of this work can be summarized in the following questions:

1) **Damage Type and Existence**: How to detect existence of tire separation?

2) **Sensor Attachment**: How to embed in-situ sensors to avoid de-bonding?

3) **Power Requirement**: Is there a way to develop self-powered sensors?

The context of smart tire in this work is defined as the development of a SHM system that (i) has self-powering capabilities, and (ii) addresses the potential of embedding sensors in the tire. Figure 1.3 shows the possible design of a next-generation smart tire. As described in previous sections, piezoelectric materials remain the most suitable class of active materials for the application of smart tires.

Figure 1.3: Artist rendering of a "Smart Tire"; Picture courtesy of Sriram Malladi

Motivated by the aforementioned problem statement, the project is divided into two components: SHM and energy harvesting. The objective of the first component is to experimentally investigate the application of impedance-based SHM on automobile tires. An approach to qualitatively understand the benefits and limitations of impedance-based SHM on an aluminum beam was first conducted before transitioning into the work on automobile tires. A high voltage impedance analyzer and the addition of electrical circuits were investigated to enhance damage identification capabilities. For the energy harvesting component, the objective is to investigate the use of ZnO piezoelectric nanowires for the development of a self-powered SHM system. An existing fabrication process to embed arrays of ZnO nanowires in carbon fiber reinforced polymer was leveraged in this work. The goal is to experimentally demonstrate power generation capabilities of ZnO nanowires. This addresses the second and third points in the problem statement above. Finally, an electro-mechanical model of a bimorph energy harvester was derived to predict the expected voltage output and to compare with experimental results. The model also provides qualitative understanding on the behavior of power generation under different loading conditions.

1.4 Thesis Organization

The following outlines a brief overview of the remainder of the thesis

Chapter 2 will focus on the SHM portion of the thesis. The benefits and limitations of the impdance-based SHM technique is discussed in this chapter, followed by a few suggestion to enhance damage identification sensitivities. Experimental testing of an aluminum beam and a tire section is discussed in this chapter.

Chapter 3 shows the derivation of a mathematical model of a linear bimorph energy harvester. Model validation and verification is also discussed in this chapter. The difference in a parallel-connected and series-connected bimorph energy harvester is discussed. Experimental and simulation work were conducted to demonstrate the power generation behavior of an energy harvester under different loading conditions.

Chapter 4 shows the experimental investigation of power generation abilities of ZnO nanowires. The fabrication process and experimental setup is discussed in this chapter. Several attempts including adding a tip mass, applying a DC voltage, and changing the geometry of the bimorph were undertaken to increase power output. Finally, a comparison between model prediction and experimental results is shown here.

Chapter 2

Impedance-based Structural Health Monitoring of Tire

2.1 Description of Impedance-based SHM

For a linear piezoelectric material, the relationship between electrical and mechanical components can be described by the following linear relations [55]:

$$\begin{bmatrix} \tau_{ij} \\ D_i \end{bmatrix} = \begin{bmatrix} C_{ijkl} & -e_{mij} \\ e_{ikl} & \varepsilon_{im} \end{bmatrix} \begin{bmatrix} S_{kl} \\ E_m \end{bmatrix} \tag{2.1}$$

where τ_{ij} is the mechanical stress, C_{ijkl} is the elastic constant measured at constant electric field, e_{mij} and e_{ikl} are the piezolectric constants, S_{kl} is the mechanical strain, D_i is the electric displacement, ε_{im} is the dielectric constant measured at constant strain, and E_m is the electric field. The direct effect of a piezoelectric material is that it produces electrical charge under mechanical stress. Likewise, its converse effect is that it produces mechanical strain under electrical field.

Impedance-based SHM uses piezoelectric wafers as collocated sensors and actuators to locally excite a structure at high frequencies. The primary concept of this active sensing technique is the energy transfer between the actuator and its host structure [30] by using both the direct and converse effects simultaneously. Liang quantitatively described an electromechanical model and the impedance method [56]. He showed that the electrical impedance of the piezoelectric transducer is directly related to the mechanical impedance of the host structure, allowing the change or damage in the structure to be detected via elecrical impedance. To conduct impedance-based SHM, a known AC voltage is used to excite the piezoelectric transducer using a frequency sweep, and at the same time, its electrical impedance is measured. The method uses high-frequency excitations, typically higher than $30kHz$, to monitor changes in in the electro-mechanical impedance, usually reflected by the presence of damage. Impedance signatures measured at a damaged status is compared to a baseline signature obtained at a known healthy state.To quantify and characterize the changes, several scalar damage metric can be used. The first statistical damage metric used is the root mean square deviation (RMSD) method:

$$M = \sum_{i=1}^{n} \sqrt{\frac{[Z_{i,1} - Z_{i,2}]^2}{[Z_{i,1}]^2}} \tag{2.2}$$

where M is the damage metric, $Z_{i,1}$ is the electrical impedance measured at the healthy condition, and $Z_{i,2}$ is the electrical impedance measured at the damaged condition. Another scalar damage metric that is commonly used with impedance-based SHM is the cross-correlation metric:

$$\rho = \frac{1}{n-1} \frac{\sum_{i=1}^{n} (Z_{i,1} - \bar{Z}_1)(Z_{i,2} - \bar{Z}_2)}{s_{Z_1} s_{Z_2}} \tag{2.3}$$

where ρ is the correlation coefficient, $Z_{i,1}$ and $Z_{i,2}$ are described above, $\bar{Z}_1$ and $\bar{Z}_2$ are the means of the electrical impedance signals, and the s terms are the standard deviations. To quantify damage, the damage metric (1-ρ) is used, where a higher number denotes a more significant change from the original condition. The cross correlation metric accounts for vertical and horizontal shifts of impedance signatures usually associated with temperature changes [9]. However, both RMSD and cross-correlation matrices are proven methods for characterizing damages and will be used interchangably in this work. The measured quantity, electrical impedance is the complex ratio of voltage to current in an AC circuit, containing both real and imaginary components:

$$Z = R + jX \tag{2.4}$$

where Z is the complex impedance, R is the real part of impedance, known as resistance, and X is the imaginary part of impedance, known as reactance. The units for all components are *Ohms*. Both real or imaginary components of the electrical impedance can be used in both statistical damage metrics. The three main parameters on the impedance-based SHM technique are frequency range, components of electrical impedance (absolute, real part, imaginary part), and sensing region of the piezoelectric transducer [28]. Each of these parameters is uniquely defined in the following sections depending on the test structure - aluminum beam, or tire section.

2.2 Experimental Setup

2.2.1 Piezoelectric Transducer

Two types of piezoelectric transducers were considered in this study. The first is the QuickPack (Model No. 1001), and the second is the Macro Fiber Composite or MFC (Model No. M2814P1). Both transducers have unique composition, most notably their substructure. A brief description of each transducer is given in this section. However, no direct comparison of the effectiveness of these transducers to conduct impedance-based SHM was investigated. Rather, they were used in two different case studies: impedance-based SHM of an aluminum beam, and impedance-based SHM of a tire section.

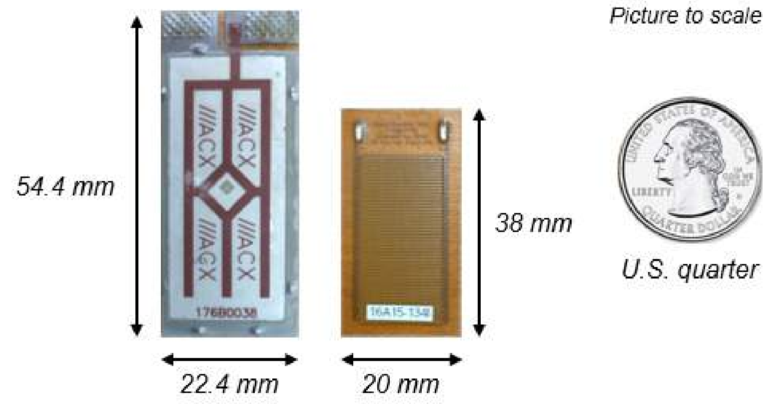

Figure 2.1: Geometric shape of piezoelectric transducers used; Left: QuickPack; Right: MFC

The QuickPack is a piezoelectric transducer manufactured by Mide Technology. It features a convenient electrical termination with large contact areas for easy electrical connection to the packaged piezo wafer. Its packaging process allows the normally brittle piezoelectric ceramic to be encapsulated in a protective layer, deceasing its rate of failure, and increasing its robustness in real world applications.

The Macro Fiber Composite (MFC), on the other hand, was first invented and developed by NASA in 1996, and was commercialized by Smart Material in 2002 [57]. The MFC contains rectangular piezo ceramic rods sandwiched between layers of adhesive, electrodes and polyimide film. The thin, surface conformable transducer can be bonded externally to various types of structures, or embedded in a composite structure. The MFC is available in d_{33} and d_{31} operational modes, known as the MFC P1 type (Elongator), and the MFC P2, P3 type (Contractor), respectively. The MFC selected for this application is a P1 type MFC, with active area of 28 x 14 mm^2, and ceramic thickness of 180 μm. This MFC will elongate up to 1800 ppm if operated at the maximum voltage rate of -500V to +1500V. The MFC is slightly more costly than the QuickPack, owing to its flexibility needed to be bonded to the curvature of a tire section.

In this work, the term QuickPack and PZT are used interchangably. The acronym PZT stands for Lead Zirconate Titanate, a commonly used piezoelectric ceramic material by Mide Technology. Here, the mention of QuickPack, or PZT should refer to the transducer on the left of Figure 2.1, and the mention of MFC should refer to the transducer on the right of Figure 2.1.

2.2.2 Impedance Measurement Techniques

Traditionally, commercially available impedance analyzers like the HP4194, or the Keysight E4990A are used to measure electrical impedance of a device under testing (DUT). Here, DUT is defined as the transducer, and/or electronics that are connected to the impedance analyzer. This can include only the QuickPack, the MFC, or either when they are attached to a host structure. These impedance analyzers use various techniques to measure electrical impedance (Figure 2.2). The I-V probe method, shown on the right of Figure 2.2, is the most straightforward impedance measurement techniques, and is suitable for the application of this work given its measurable impedance and frequency range [58]. The method consists of a tunable resistor connected in series with the DUT, allowing current measurements to be taken, which will be used to calculate the impedance of the DUT. For impedance measurements involving an excitation of 1V, the Keysight E4990A was used.

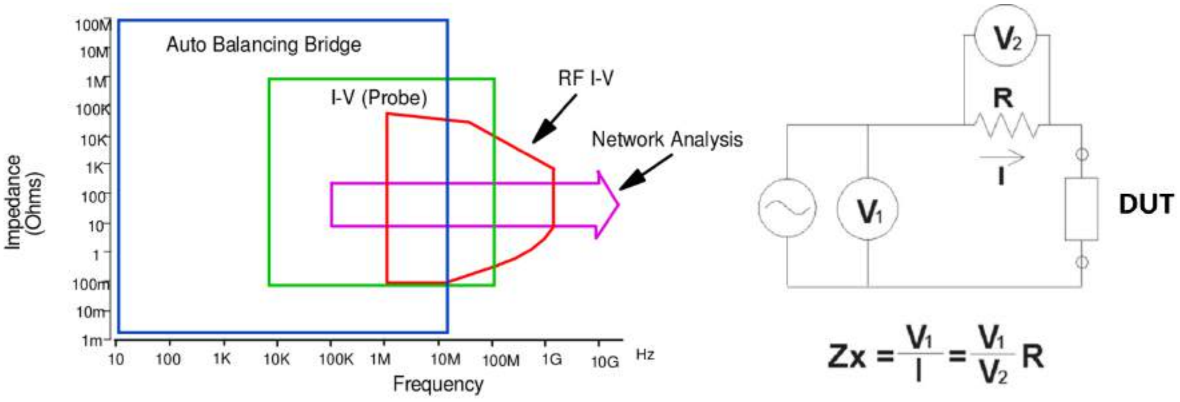

Figure 2.2: Left: Impedance measurement techniques; Right: Schemetic of the I-V probe method [58]

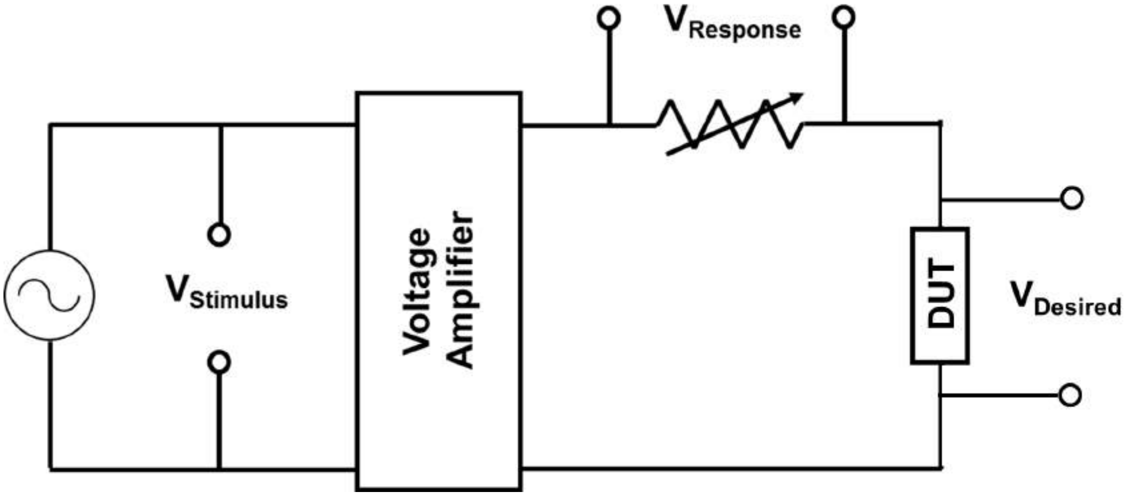

Figure 2.3: Schemetic of modified I-V probe circuit for high voltage impedance analyzer

However, commercially available impedance analyzers like the E4990A can only excite the DUT to up to 1V. To interrogate structures with high damping, low stiffness, or under noisy environments, a high voltage impedance analyzer could be used. This requires a setup involving a voltage measurement circuit, voltage amplifier, signal analyzer with a source channel and fast fourier transform (FFT) capability, along with a tunable resistor in series. A NI-PXI Digital Multimeter (DMM) system with a NI-6115 card (12-Bit, 10 MS/s/ch, 4-Input/2-Output) was used to simultaneously generate a voltage signal and measure the voltage drop across the resistance in series with the DUT. A NF High Speed Bipolar Amplifier 4052 (+/-150ACV, up to 500 kHz) was used to amplify the voltage generated by the DMM. The gain can be adjusted, and will be selected based on the application and voltage range. The DMM measures the voltages and applies FFT to output the complex frequency response function $V_{Stimulus}/V_{Response}$. The complex impedance can then be calculated with the following equation:

$$Z = ((\frac{V_{Stimulus}}{V_{Response}})G - 1)R \tag{2.5}$$

where G is the gain, and R is the resistance. The resistance is a crucial parameter that needs to be tuned in order to obtain clean impedance signatures. If the resistance is too high, then the voltage drop across the the DUT, $V_{Desired}$ is reduced, countering the purpose of the high voltage impedance analyzer setup. This may reduce damage detection sensitivity which will be discussed later. Also, the upper limit of the resistor is constrained by the maximum voltage analog input of the DMM $(+/-10V)$. If the resistance is too low, the result will be a low voltage measurement across the resistor, leading to low signal-to-noise ratio. Since the impedance of the piezoelectric sensors considered here is frequency dependant, the frequency band was subdivided into intervals, and a unique resistor value for each interval was selected before the electrical impedance was measured. Considering the aforementioned factors that affect ideal resistor value, the target voltage drop across the resistor was set to be $1V$, allowing a high potential difference across the DUT when the high voltage impedance analyzer was opted, but at the same time ensuring the voltage drop across the resistor, $V_{Response}$ is well above the noise floor. The steps to approximate the resistor value for each frequency interval are outlined below:

1) Measure the average impedance of DUT, Z_{avg} with the E4990A

2) Calculate the value of the tunable resistor (using Ohm's Law):

$$R = \frac{Z_{avg}}{V_{desired}} \tag{2.6}$$

where $V_{desired}$ is the desired voltage drop across the DUT. This can be increased to a maximum of $100V$ in the MFC. While the MFC is designed to operate with from -500 V to +1500 V capacity, it has a maximum current capacity of 50 mA. At high frequency regions, the impedance of the MFC is reduced, reaching its maximum current capacity.

Another limitation of the impedance-based SHM technique is that only one probe can be used at a given time; meaning the DUT will have to be switched out to obtain electrical impedance signatures of other sensors. This could be a time-consuming effort if a large sensing area is desired, which will require an array of sensor networks. This work will also investigate the connection of multiple sensors (both QuickPack and MFC) in series, and in parallel, and the effects they have on the sensitivity of damage identification.

It is worth mentioning that the impedance obtained by equations 2.4 and 2.5 are complex quantities, of which its absolute magnitude, real part, or imaginary part could be used for damage identification. The inverse of electrical impedance, known as electrical admittance, is also commonly used by different authors in the field of impedance-based SHM. Like impedance, the electrical admittance contains a real part, and an imaginary part. In this work, both electrical impedance and electrical admittance were used to quantify damage. The author will specify which signatures were used for each corresponding tests. For electrical admittance, equations 2.4 and 2.5 are replaced by

$$Y = G + jB \tag{2.7}$$

$$Y = Z^{-1} \tag{2.8}$$

where Y is admittance, G is conductance, and B is susceptance. There is no qualitative difference in using either impedance or admittance, as long as it is kept consistent for each test.

2.2.3 Damage Identification Enhancement with Electrical Circuit

The presence of electrical resonances and anti-resonances in the electrical impedance of a piezoelectric transducer is the result of the electro-mechanical coupling of the piezoceramic material and its host structure. The damage effect is reflected at these resonant peaks in the impedance curves. Depending on the host structure, there may be an abundance of these resonant peaks at high frequencies, or there may be limited or none. The typical circuity elements such as inductors, resistors, and capacitors are analogous to structural elements such as mass, damping, and stiffness in the mechanical system [59]. Several researchers such as Inman have seek to model the equivalent electrical impedance of a piezoceramic transducer attached to a structure by using circuitry elements [60]. Figure 2.4 shows one example of an equivalent circuit to model the impedance resonance and anti-resonance. Using added circuitry network in parallel or in series with the piezoelectric sensor bonded on the structure of interest as the effective DUT, one can favorably adjusts the additional resonant peaks in the electro-mechanical system. This method is particularly useful when the structure of interest is a tire section because these resonant peaks can be used to detect and characterize the presence of damage.

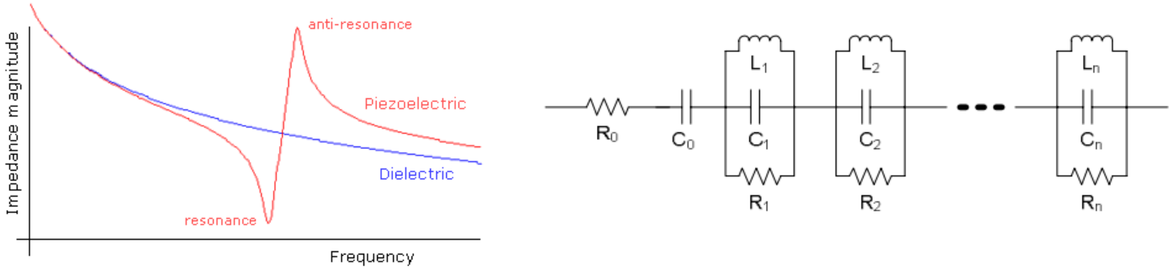

Figure 2.4: Left: Piezoelectric impedance due to electro-mechanical coupling [61]; Right: The "Easy Model" used to create the equivalent circuitry model of a piezoelectric impedance signature [60]

In this work, the "Easy Model" depicted in the right of Figure 2.4 was adopted [60]. A tunable inductor, capacitor and resistor in parallel were connected in series with the piezoelectric sensor as an effective DUT. To adjust the peak location, and its magnitude on the impedance signature, the following equation is used:

$$Z_{RCL} = \frac{1}{\frac{1}{R_1} + \frac{1}{j\omega L_1} + j\omega C_1} \tag{2.9}$$

where Z_{RCL} is the impedance of the effective RCL circuit, R_1 is the resistor value, L_1 is the inductor value, and C_1 is the capacitor value. Figure 2.5 shows the effectiveness of equation 2.9 to predict the peak location and its magnitude. Here, the measured impedance signature was obtained using the E4990A Impedance Analyzer.

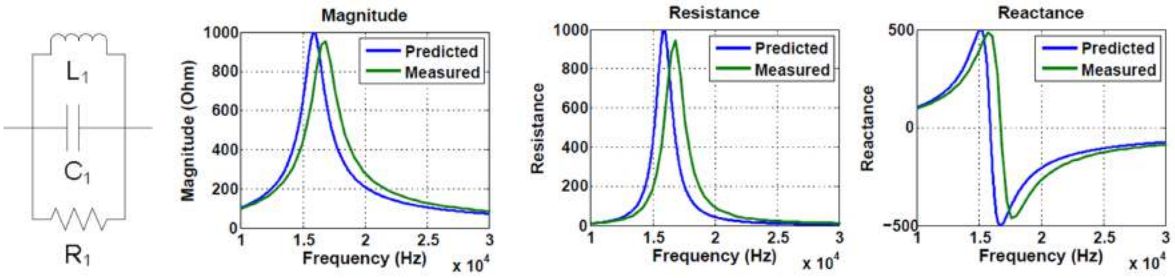

Figure 2.5: Impedance (Magnitude, Real part, and Imaginary part) of a RCL circuit in parallel

2.3 Results

2.3.1 Aluminum Beam with QuickPack

Usually, an array of piezoelectric sensors is required to conduct SHM of a desired structure. This test seeks to understand the damage identification capability when multiple sensors were connected in parallel. Here, the impedance analyzer with a low AC voltage ($1V$) was used. Hence, series connection was not considered, because pizeoelectric sensors in series connection will cause the voltage drop across each sensors to be distributed, reducing the damage identification capability. Figure 2.6 shows the desired structure to be interrogated, however, a simple aluminum beam was used to understand the behavior of the change in impedance measurements when multiple sensors were connected in parallel.

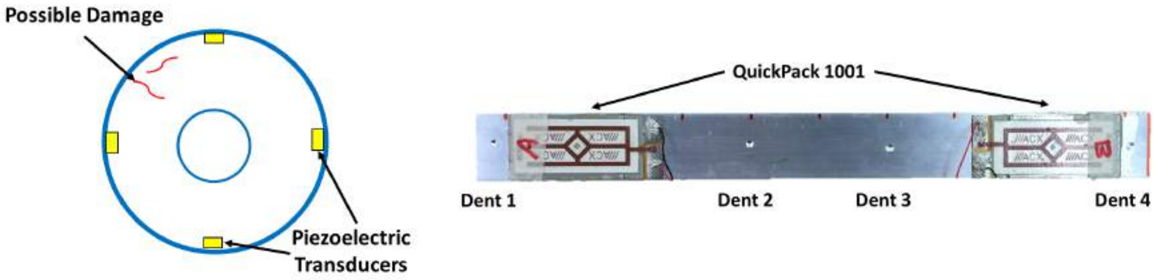

Figure 2.6: Left: Structure of interest with an array of sensors and random damages; Right: Representative structure setup with two QuickPack sensors

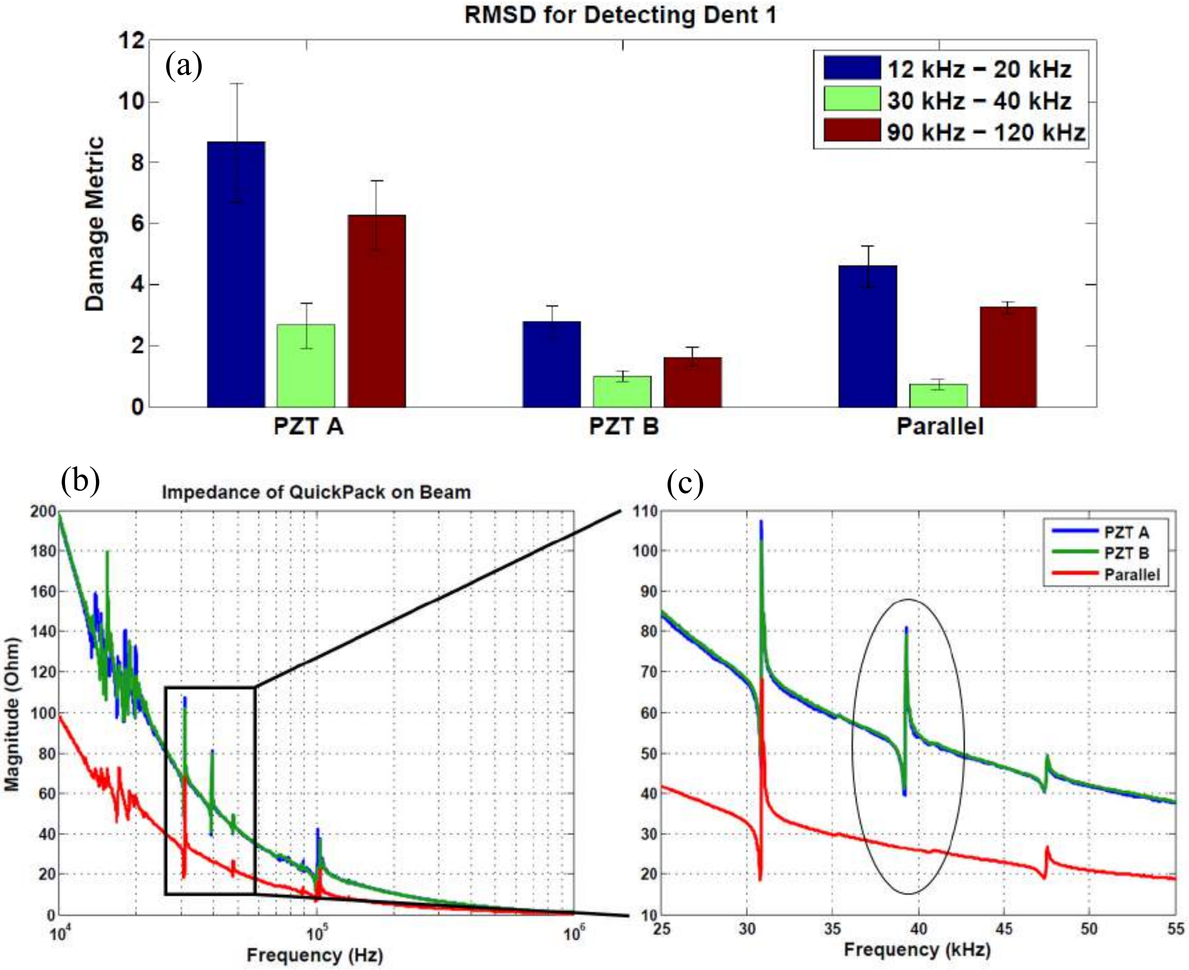

Figure 2.7: (a) Scalar damage metric demonstrating ability of PZT A, PZT B, and parallel connection to detect presence of dent 1; (b) - (c) Impedance signature of each configuration under healthy state (baseline)

The impedance measurement were obtained from $1kHz$ to $1MHz$. However, for statistical damage metric calculations, three frequency ranges were identified and the root mean square deviation (RMSD) definition was used to quantify the change in impedance signatures at each frequency regions caused by the presence of damage. The three frequency ranges were $12kHz - 20kHz$, $30kHz - 40kHz$, and $90kHz - 120kHz$. First, baseline measurements were taken when there were no dents on the aluminum beam. Then, progressive permanent damages (Dent 1, 2, 3, and 4) were induced. In between each damage progression, the electrical impedance of individual PZTs (QuickPack) and those connected in parallel were measured. Three measurements were taken for each case and their average calculated. To understand the ability of PZTs in parallel connection to detect damage, the RMSD damage metric is shown in Figure 2.7. A higher damage metric for the first and last frequency range indicates those frequency ranges to be more sensitive to damage. PZT A shows a higher damage metric because dent 1 occurred closer to PZT A than it is to PZT B. It is noted that for the parallel configuration, the damage metric lies in between the ones obtained by the individual sensors, suggesting a trade off between sensitivity and interrogation time (switching out the DUT). The reduction in damage detection sensitivity in the parallel configuration can be explained by Figure 2.7 (b) - (c), where one of the mechanical resonance mode disappears when the two PZT were connected in parallel, causing the loss of information as compared to measuring the impedance of individual sensors.

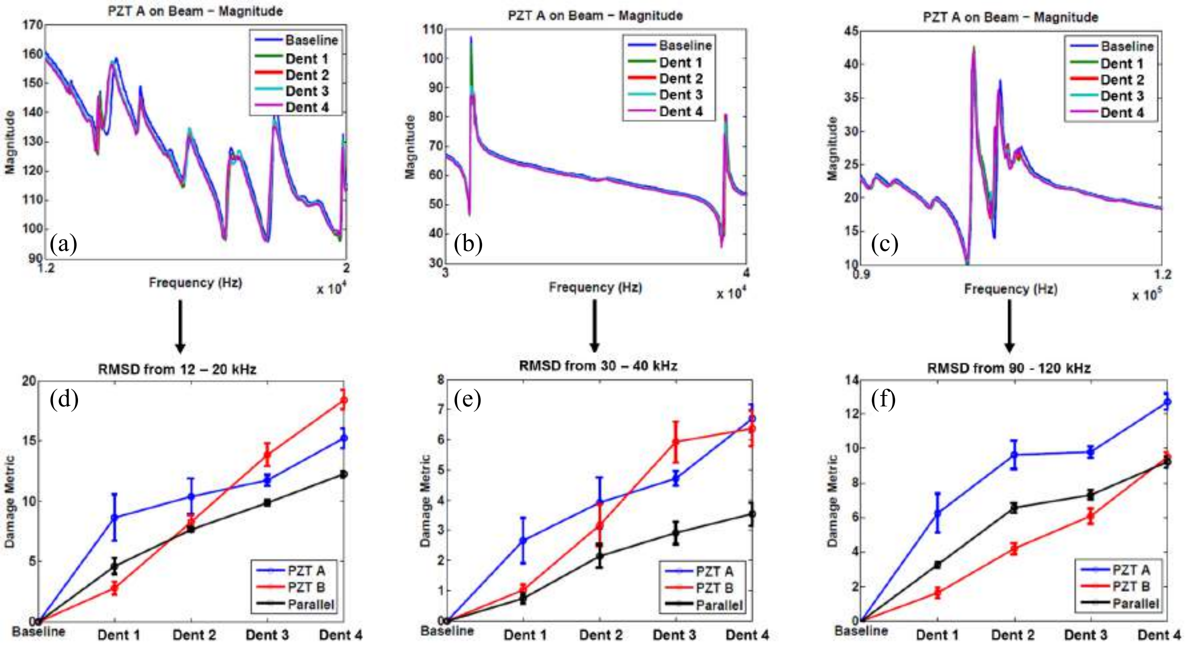

Figure 2.8: (a) - (c) Impedance signatures at several frequency range; (d) - (f) Damage metric using root mean square deviation (RMSD)

The ability of PZT A, PZT B, and their parallel configuration to detect progressive damage is represented in Figure 2.8. The impedance signatures at each state (Dent 1, 2, 3, and 4) were compared to the baseline measurement (Healthy state). It is observed that for all three frequency ranges, the damage metric increases, indicating an increasing severity of damage as the number of dents accumulate. For dent 1 and 2, PZT A shows a higher damage metric because the dent locations occurred closer to PZT A than it is to PZT B. For dent 3 and dent 4, PZT B shows a higher damage metric because the dent locations occurred closer to PZT B for the first two frequency ranges. It is again noted that for the parallel configuration, the damage metric lies either in between the ones obtained by the individual sensors, or below them. However, it does show a similar trend in increasing damage metric, proving its ability to detect severity of damage. This test also suggests the ability of multiple sensors connected in parallel to detect existence of damage globally;

although to detect damage locally with high sensitivity will require measuring the electrical impedance of individual sensors. This reaffirms the trade-off between damage detection sensitivity and interrogation time that needs to be taken into account when designing an impedance-based SHM system.

2.3.2 Aluminum Beam with MFC

The overall objective of this test is to test the benefits of using a high voltage impedance analyzer in identifying damage. It was demonstrated that since most structural defects such as cracks and loose joints are nonlinear in nature, tracking the damage induced non-linearities by impedance-based SHM could prove beneficial [62]. Albakri et al. [62] successfully observed nonlinear stiffness and damping in a numerical simulation of a simple free-free beam, and in experimental investigation of a lap joint. This work serves as a stepping stone in understanding the variables involved in tuning the parameters of the high voltage impedance analyzer on a linear structure (free-free aluminum beam) before transitioning to a material with high damping and low stiffness (tire section).

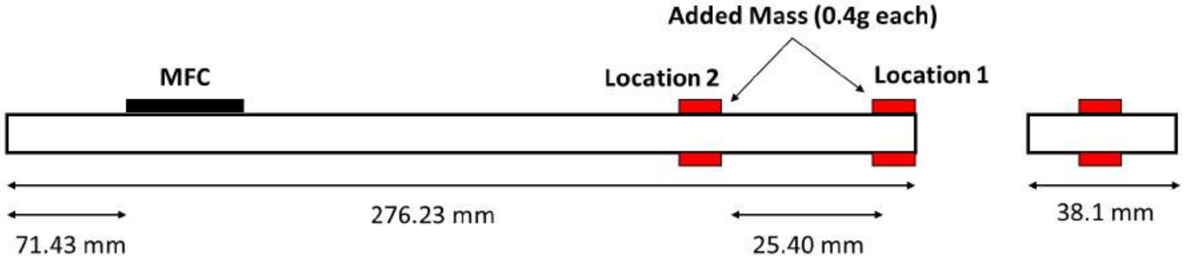

Figure 2.9: Schemetic of MFC and damage (simulated with added mass) location for high voltage impedance test

The first two tests were conducted to understand the effect of voltage selection and resistance selection based on the setup described in Section 2.2.2. For these tests, one frequency range was considered: $55.9kHz - 56.7kHz$. This region was selected because it contains sufficient dynamic interaction that is needed for analysis. It should also be noted that the impedance measurements were taken when the MFC was attached to the beam without any added mass, termed the healthy state. The gain for this test was set at ×20. The two tests are categorized as "Constant resistance, varying voltage" and "Constant voltage, varying resistance" tests. For the first test, the resistance was set at $R = 100\Omega$, and the input voltage was set at $V_{Stimulus} = 0.25V, 0.75V, 1.25V, 2.5V, 5V$, resulting in the amplified voltage to be $5V, 15V, 25V, 50V$, and $100V$, respectively. For the second test, the input voltage was set at $V_{Stimulus} = 2.5V$, resulting in an amplified voltage to be $50V$. Here the resistance was set at $R = 20\Omega, 100\Omega, 150\Omega, 200\Omega, 250\Omega$.

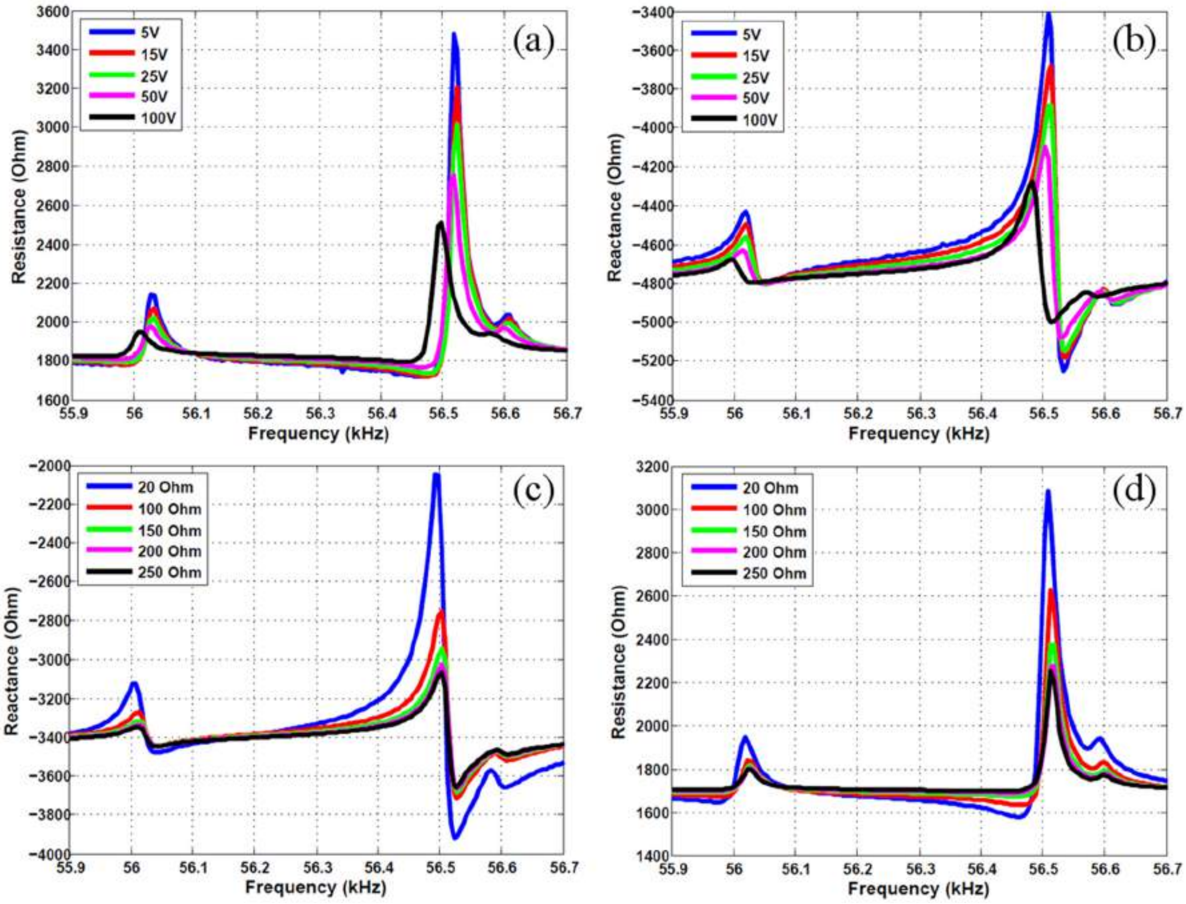

Figure 2.10: Resistance and reactance signatures; (a) - (b): Constant Resistance, Varying Voltage Test; (c) - (d): Constant Voltage, Varying Resistance Test

For the "Constant resistance, varying voltage" test, and for cases $5V$ to $50V$, the resonant peak locations remained the same while its magnitude decreased. However, when the voltage was increased to $100V$, there was a significant leftward shift in resonant frequencies suggesting the point where the structure starts to behave in a nonlinear behavior. For the "Constant voltage, varying resistance" test, there was a rightward shift in resonant peak locations, and a decrease in magnitude as the resistance was increased. These test show that the voltage and resistance are introduced as two additional variables in the electro-mechanical system. The subsequent tests will adjust these degrees of freedom according to the description in Section 2.2.2.

The next tests are SHM tests, where different effective voltage drop across the DUT, $V_{desired}$ were tuned to be $V_{desired} = 1V, 10V, 25V, 50V, 100V$. The value of R and $V_{Stimulus}$ can be calculated by following the procedures under Section 2.2.2. For this test, the frequency range $10kHz$ to $80kHz$ was subdivded into 7 subranges with $10kHz$ intervals, and a gain of ×100 was used. Table 2.1 shows the unique resistor values calculated for each frequency ranges, and for each $V_{desired}$ cases. It can be noted that for the $1V$ case, upon increasing frequency ranges, the resistor values decreases. Such decrease was proportional to the decrease in average impedance of the DUT, so that the average value of $V_{response}$ was maintained at 1V. As $V_{desired}$ increases, R decreases. For all cases, the average voltage drop across the resistor was $1V$.

Table 2.1: Resistor (Ohms) values used for each frequency range and voltage selection

	1V	10V	25V	50V	100V
10 - 20 kHz	12879	1288	515	256	129
20 - 30 kHz	7700	770	308	154	77
30 - 40 kHz	5531	553	221	111	55
40 - 50 kHz	4333	433	173	87	43
50 - 60 kHz	3561	356	142	71	36
60 - 70 kHz	3036	304	121	61	30
70 - 80 kHz	2643	264	106	53	26

The first SHM test was conducted to detect the existence of damage. Here, two magnets of mass 0.4g each were added to both sides of Location 1 as shown in Figure 2.9. The test matrix was to sweep all 7 frequency ranges and 5 voltage ranges outlined in Table 2.1. Here, the cross-correlation damage metric, equation 2.3 was used for both the real part and imginary part of the impedance signature. The damage metrics reported in the following figures were calculated following $(1-\rho)$ definition. Hence, an increase in damage metric value corresponds to an increase in damage (or increase in damage sensitivity).

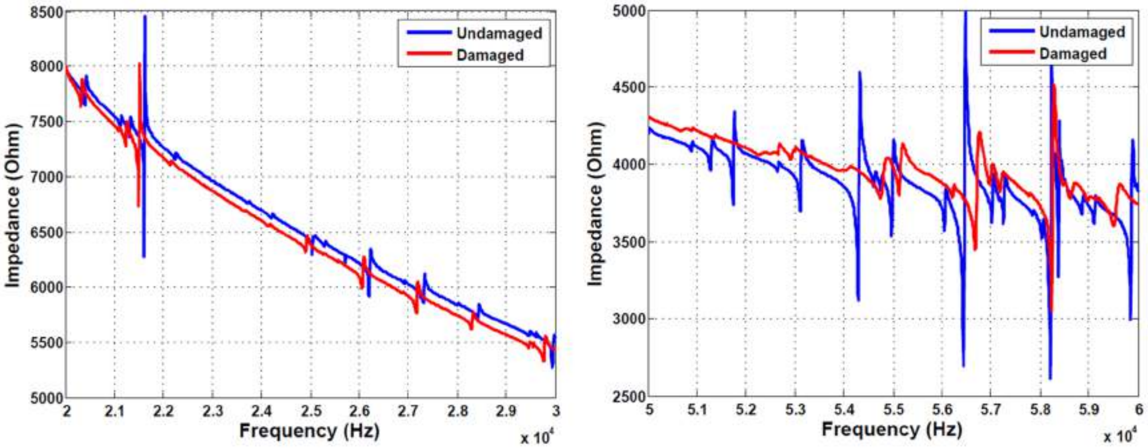

Figure 2.11: Impedance signature taken with $V_{Desired} = 100V$; Left: 20 - 30 kHz showing less resonant peaks, indicating lower sensitivity to damage; Right: 50 - 60 kHz showing more resonant peaks, indicating higher sensitivity to damage

Figure 2.12 and 2.13 show the cross-correlation damage metric for detecting the presence of damage using the real part, and imaginary part of impedance, respectively. It should be noted that for the 1V case, data for 60 - 70 kHz was incomplete, due to experimental error. However, a quick observation of all voltage cases show that 50 - 70 kHz was more sensitive to damage than 10 - 30 kHz. This is consistent with the general impedance-based SHM approach where higher frequencies are preferred. Figure 2.11 compares the impedance signature of a less sensitive frequency range to a more sensitive frequency range.

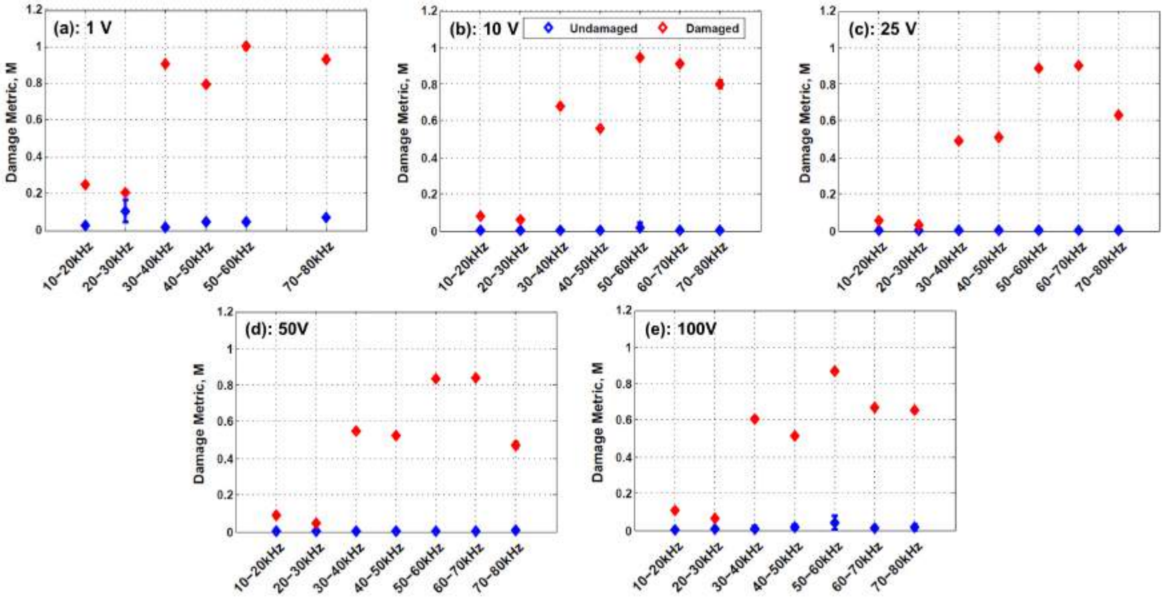

Figure 2.12: Cross-correlation Damage Metric to detect Damage Existence using Resistance; (a) 1V; (b) 10 V; (c) 25 V; (d) 50 V; (e) 100 V

Investigating the effect of voltages on each frequency range in 2.12, the damage metric value obtained using the real part of the impedance signature decreases as voltage was increased, indicating a drop in damage detection sensitivity. However, for the damage metric value obtained using the imaginary part of the impedance signature (2.13), there is a nonlinear increase in damage metric as voltage was increased. This phenomena was investigated further by shifting the two magnets from location 1 to location 2 as illustrated in Figure 2.9. The impedance signatures were remeasured, and the cross-correlation damage metric values calculated. This test was done for one frequency region only: 40 - 50 kHz. Figure 2.14 shows the damage metric for damages at location 1 and at location 2. Observing the damage metric values found using the real part of the impedance signatures, the damage metric difference between location 1 and location 2 increases as voltage increases, indicating sensitivity to location. This suggests the use of high voltage impedance analyzer for better localization of damage. The same phenomena was also observed for the case with imginary part of the impedance signature, where the difference of the damage metric increases as voltage increases. It should also be noted that for both cases, the damage metric was approaching a horizontal asymptote, indicating diminishing returns as voltage was increased.

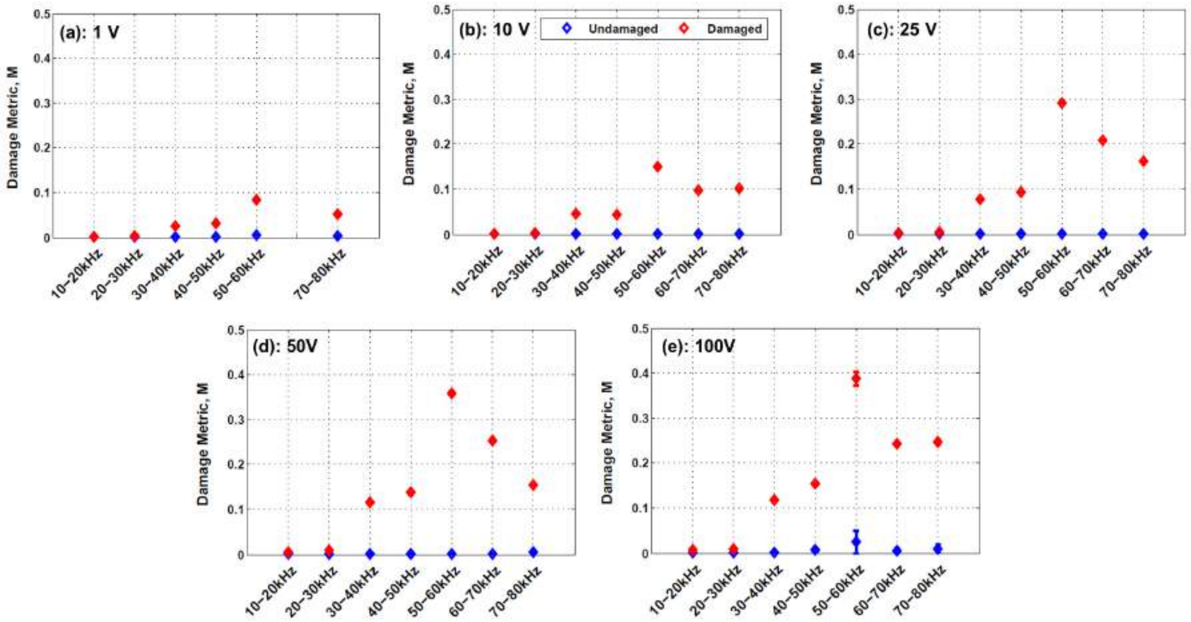

Figure 2.13: Cross-correlation Damage Metric to detect Damage Existence using Reactance; (a) 1V; (b) 10 V; (c) 25 V; (d) 50 V; (e) 100 V

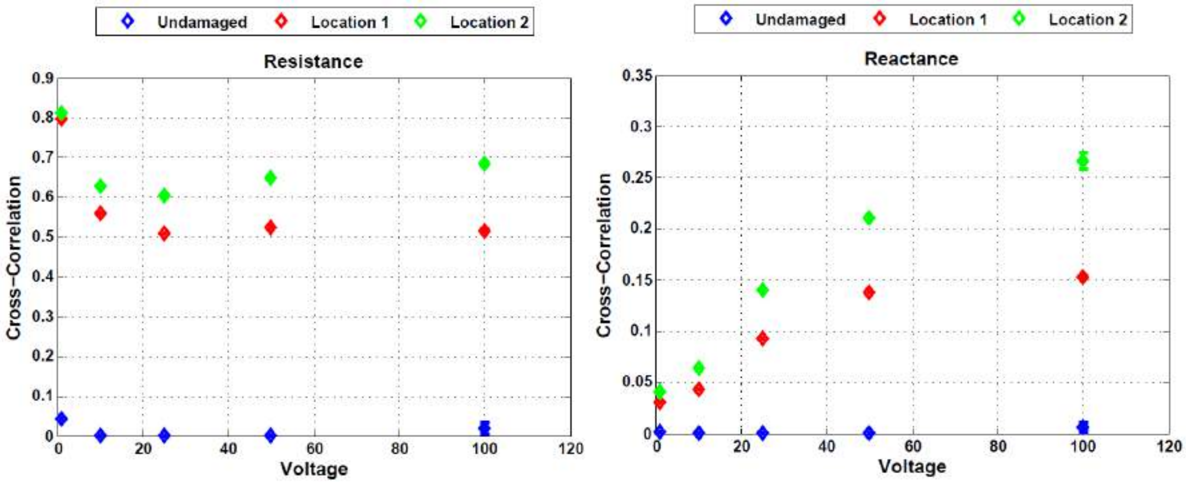

Figure 2.14: Cross-correlation Damage Metric to detect Damage at Location 1, and Location 2; Left: using Resistance; Right: using Reactance

Investigating further on the impedance signatures shown in Figure 2.15, it can be noted that the resonant peak magnitudes for location 1 are significantly smaller than the peak magnitudes for the undamaged case. This can be attributed to the added damping by the glue that was used to add the mass at location 1. Observing the impedance signatures for location 2, the peaks are more comparable to the undamaged case, signifying an inconsistency in the application of glue when the masses were added. It is also noted that the difference between impedance of location 1 and 2 for 100V is more apparent than the difference of location 1 and 2 for 1V, as confirmed by the damage metric calculations shown in Figure 2.14. This suggests the ability of a high voltage impedance analyzer to provide insight on damage type, in addition to damage location.

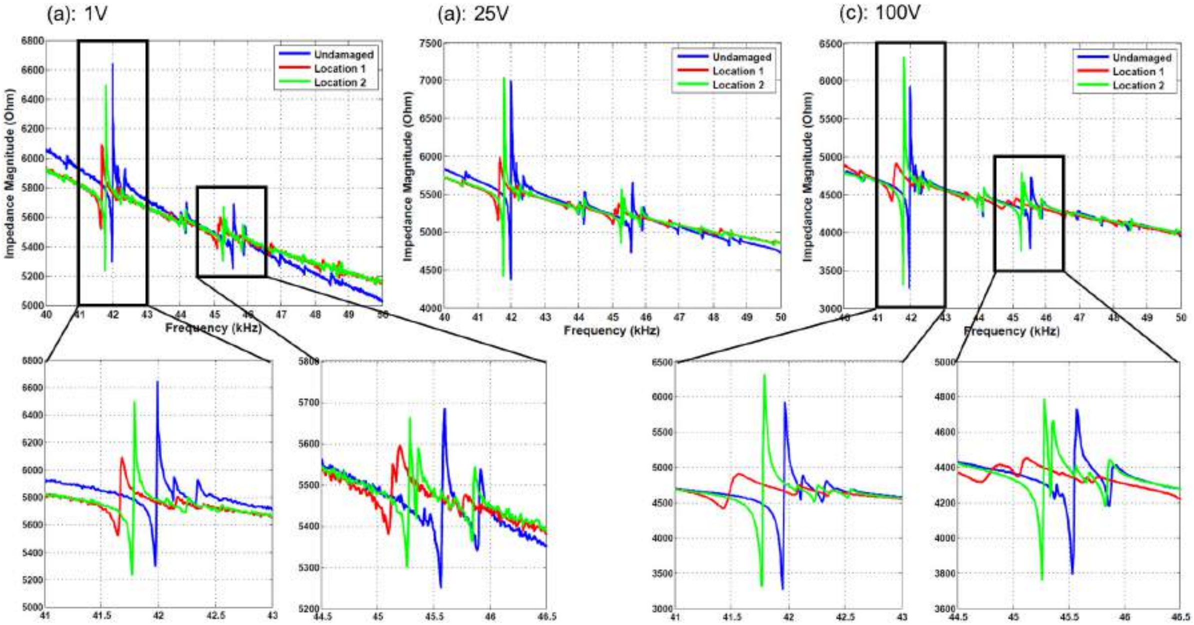

Figure 2.15: Impedance signatures taken at baseline, mass added at location 1 and at location 2; (a) $V_{Desired} = 1V$; (b) $V_{Desired} = 25V$; (c) $V_{Desired} = 100V$

2.3.3 Tire Section with MFC

In this section, two MFC sensors were attached to a tire section as shown in Figure 2.16. Unlike the case of the aluminum beam, or other structures with high stiffness or low material damping, the impedance-based SHM technique becomes limited when applied on a tire section. In previous sections, when impedance-based SHM was applied on an aluminum beam, there exists an abundance of resonant peaks at high frequencies. However, when the MFC was attached to a tire section, the expected resonant peaks are drastically attenuated as shown in Figure 2.17. This is associated to the increase of material damping, a dynamic property that is dependant on the medium of itself. For example, the representative damping ratio of rubber is five times more than metals in their elastic range, as reported in [63].

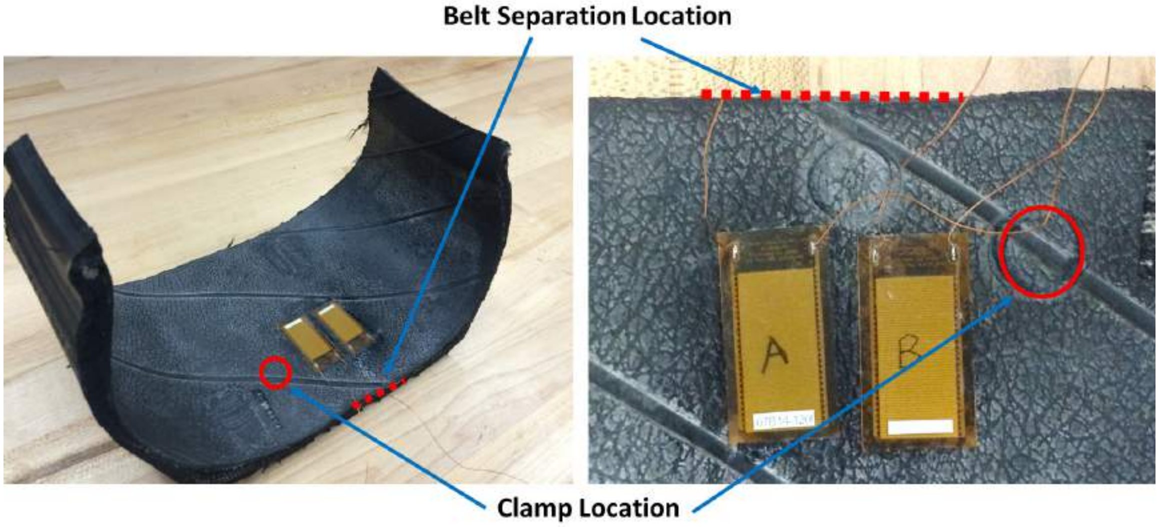

Figure 2.16: Tire Section with two MFC sensors with target representative damage locations

Due to the attenuation of resonant peaks in the impedance signature, a preliminary test was conducted to prove the existence of an electrico-mechanical coupling between the sensor and its host structure. Each sensor, MFC A and MFC B were treated as individual DUT after they were bonded to the tire section. The frequency range considered here was 1 - 20 kHz. The impedance measurement were taken for the baseline, termed unclamped state. Then, a clamp was placed on the location shown in Figure 2.16. Each state is an average of three measurements. The impedance measurement taken after this step is termed the clamped state. Figure 2.18 shows the horizontal shift in the phase of the clamped state. It is also noted that the shift was more predominant in MFC B, due to its closer location to the clamp than was MFC A.

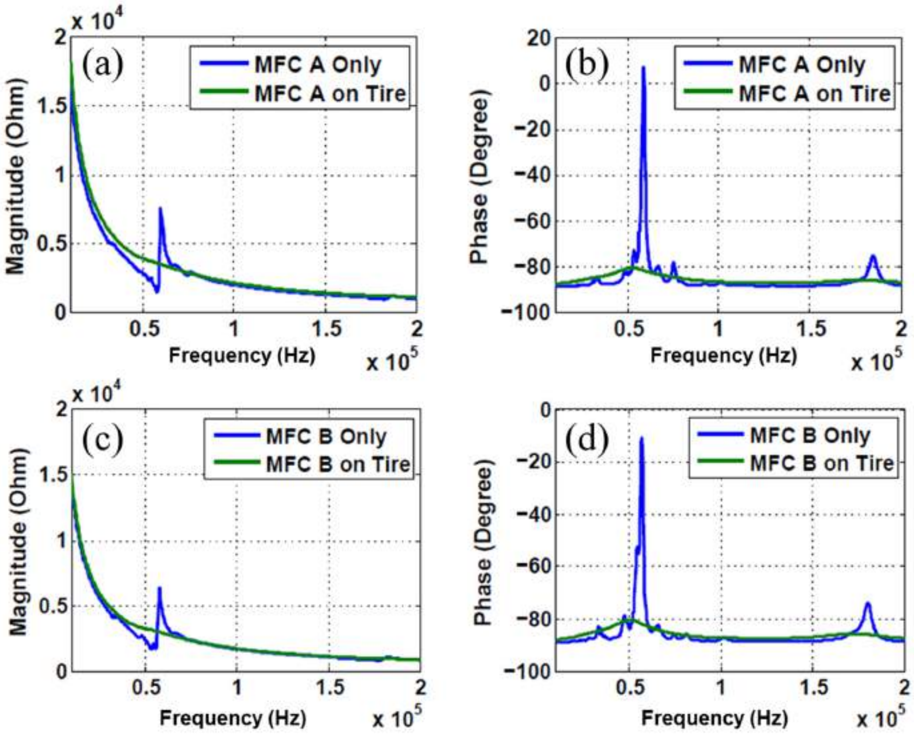

Figure 2.17: Impedance signature of (a) - (b) MFC A, (c) - (d) MFC B

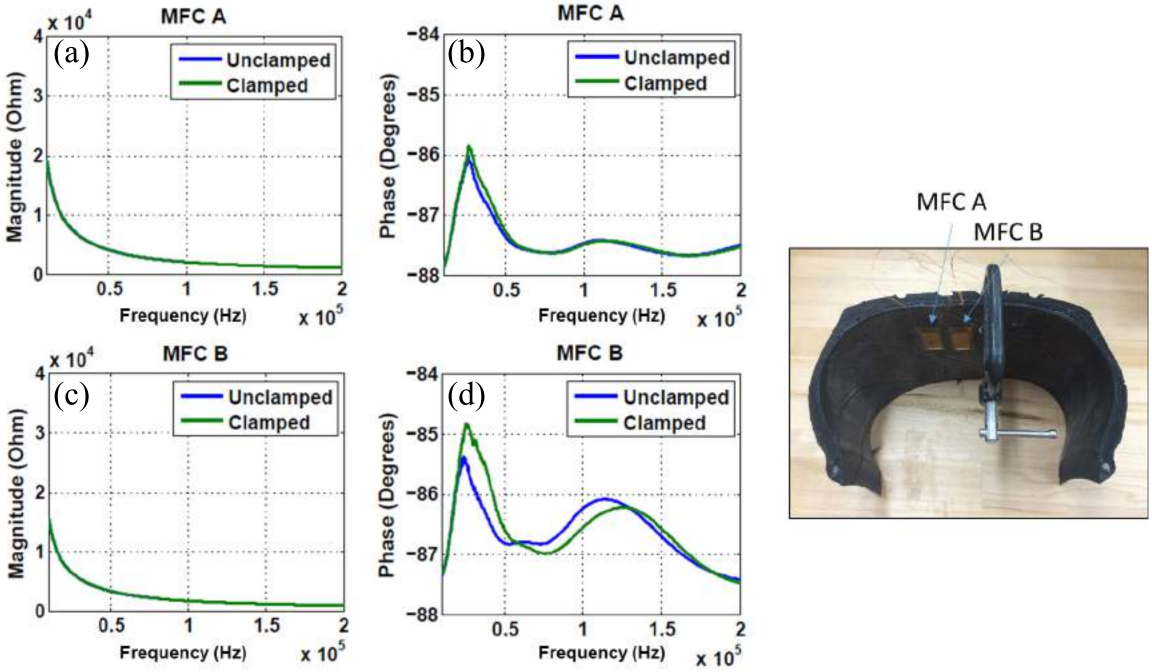

Figure 2.18: Effect of clamp on impedance signature of (a) - (b) MFC A, (c) - (d) MFC B

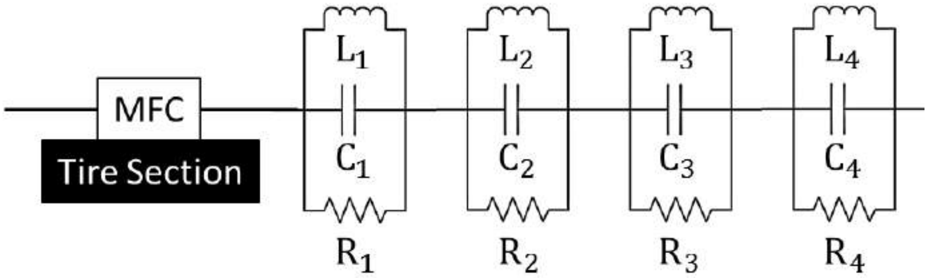

Figure 2.19: Schemetic of effective DUT with the addtion of RCL circuits

To take advantage of the enhanced damage identification method using added electrical circuits described in Section 2.2.3, four sets of resistors, capacitors, and inductors were identified. These circuits are termed RCL circuits. The values of these electrical components are shown in Table 2.2. First, MFC A was connected in series to RCL_1, then connected in series to RCL_1, RCL_2, RCL_3, and RCL_4. The excitation voltage was 1 V. The frequency range considered here was 10 - 50 kHz. Three admittance measurements were taken for the baseline, termed healthy state. Then three more admittance measurements were taken after a separation on the belt area of the tire section was induced, termed damaged state.

Table 2.2: Values of electrical components used for each frequency ranges and voltage selection

	Resistor (Ohm)	Capacitor (nF)	Inductor (mH)
RCL_1	46.1k	2.31	47
RCL_2	46.2k	0.95	47
RCL_3	0.825M	0.21	100
RCL_4	0.819M	0.13	100

Figure 2.20 shows that while with one added RCL there is a small increase in damage metric during the damaged state, the shift in the resonant peaks can hardly be seen. However, when four added RCL circuits were used, the damage metric increases significantly, as confirmed by the visually identifiable shift in the resonant peaks in the admittace signature. It should also be noted that the resonant peaks that do shift due to damage seem to be on the higher end of the frequency range, suggesting the need to tune the added RCL circuit to favor such behavior.

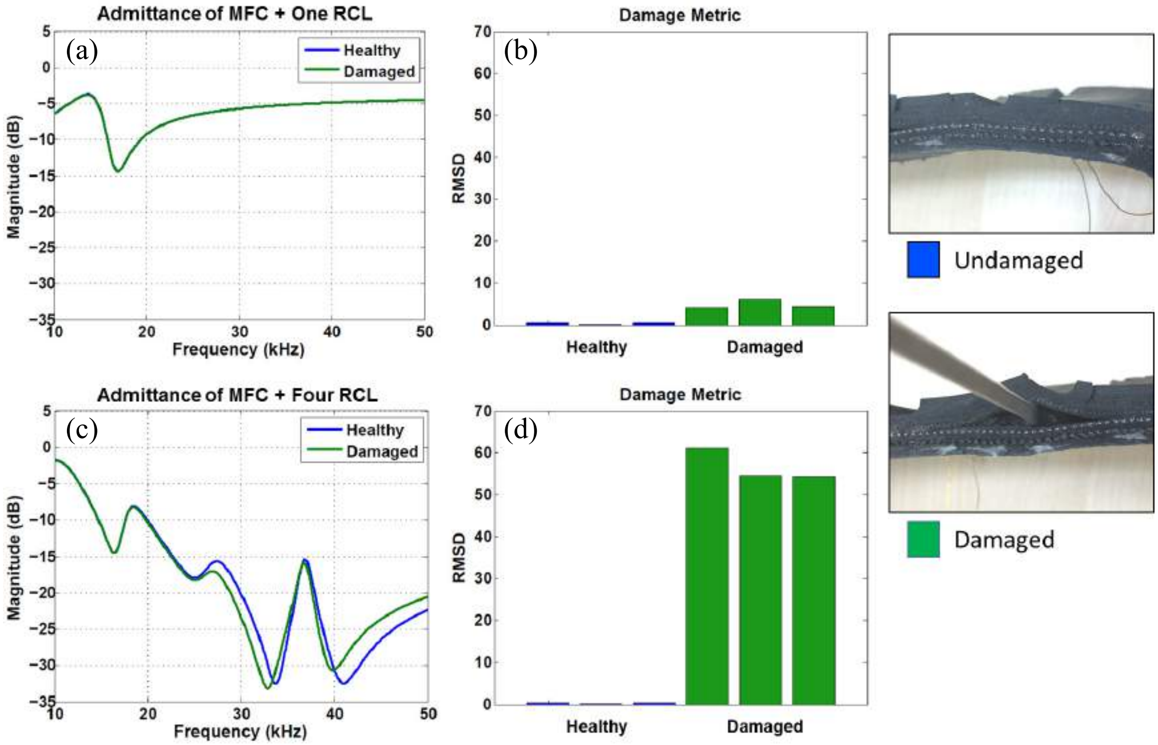

Figure 2.20: Damage Detection with (a) - (b) One added RCL circuit, (c) - (d) Four added RCL circuits

Chapter 3

Mathematical Modeling of Base Excitation Cantilever Energy Harvester

3.1 Modeling Assumptions

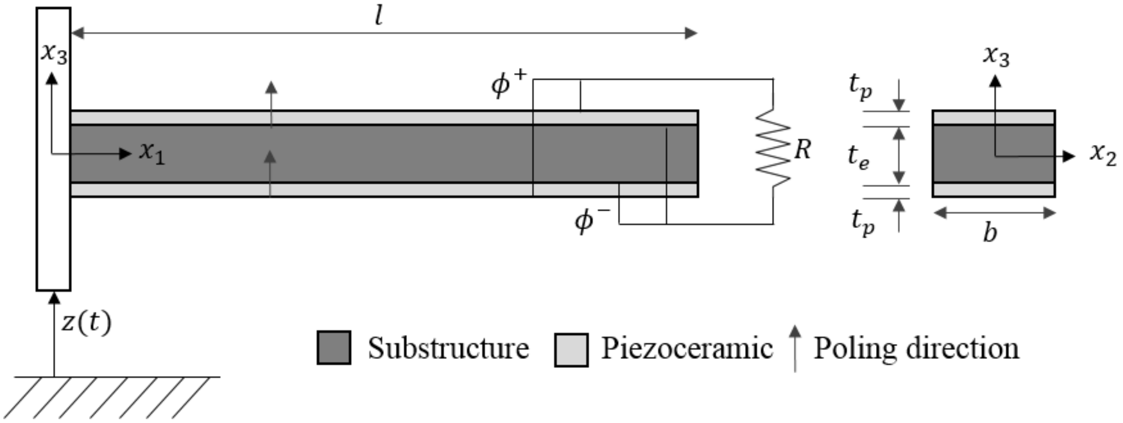

Figure 3.1: Bimorph piezoelectric energy harvester configuration

The energy harvester model is based on a bimorph cantilevered beam configuration as illustrated in Figure 3.1. The length-to-thickness aspect ratio of the composite beam is large; hence neglecting shear deformation and using Euler-Bernoulli beam assumptions. The composite beam is assumed to exhibit linear-elastic material behavior, subjected to small deformation. The electro-mechanical relationship of linear piezoelectric materials (Eqn. 2.1) is also assumed. The top and bottom piezoelectric layer is bonded perfectly on the substructure, and covers the entire length of the beam. The piezoelectric layers are poled in the same thickness direction. Harmonic base excitation with displacement $z(t)$ in the transverse direction is applied. Both viscous air damping and hysteretic damping were subsequently added via modal damping when the model is correlated with experimental work.

3.2 Electromechanical Modeling of Distributed - Parameter Bimorph Harvester

3.2.1 Extended Hamilton's Principle

Using the Extended Hamilton's principle, nonconservative forces were taken into account for the piezoelectric energy harvester. The Extended Hamilton's principle states that

$$\delta \int_{t_0}^{t_1} (T - V_H)dt + \int_{t_0}^{t_1} \delta W_{nc} dt = 0 \tag{3.1}$$

for all admissible variations δq of the true motion q where T is the kinetic energy, V_H is the electric enthalpy, and δW_{nc} is the virtual work performed by nonconservative forces. The kinetic energy for a Euler-Bernoulli's Beam is used for the kinetic energy of the composite piezoceramic beam [39]. For a piezoelectric beam configuration, the electric enthalpy can be shown to be [64]

$$V_H = \frac{1}{2}\int_0^L YI(w'')^2 dx_1 + \int\int\int e_{31}E_3 x_3 (w'')dV - \frac{1}{2}\int\int\int \varepsilon_{33}^S E_3^2 dV \tag{3.2}$$

where YI is the effective bending stiffness of the composite beam including the piezoelectric layer, w is the deflection, e_{31} is the plane-stress piezoelectric constant for a thin beam, x_3 is the transverse direction, L is the length of the composite beam, and ε_{33}^S is the electric permittivity constant. Given the potential difference, $V = \phi^+ - \phi^-$, one can set $\phi^- = 0$ and use the approximation of electric field,

$$E_3 = -\frac{\partial \phi}{\partial x_3} \tag{3.3}$$

to rewrite equation 3.2 in the following form

$$V_H = \frac{1}{2}\int_0^L YI(w'')^2 dx_1 - \int_0^L Qe_{31}\frac{V}{t_p}(w'')dx_1 - V^2\int_0^L \frac{A_p \varepsilon_{33}^S}{t_p^2} dx_1 \tag{3.4}$$

where Q is the subtraction of the first moment of area of the bottom piezoceramic layer from the first moment of area of the top piezoceramic layer, and $A_p = t_p \times b$. Considering no external applied stress, the nonconservative force term in equation 3.1 can be approximated by

$$\delta W_{nc} = \int\int (-\bar{\sigma}\delta\phi)da \tag{3.5}$$

where $\bar{\sigma}$ is the charge distribution. With two piezoceramic layers on the top and bottom of the composite beam, and using the fact that $\phi^- = 0$, the total nonconservative forces can be approximated by

$$\delta W_{nc} = -2q\delta V \tag{3.6}$$

where q is the electric charge. When nonconservative forces are not considered, the formulation of Hamilton's Principle for a composite piezoceramic beam is similar with the formulation for the classical Euler-Bernoulli's Beam [39], except with the addition of the last two terms on the right hand side of equation 3.4. Using the fact that the variation operator $\delta(\cdot)$ obeys the chain rule, and that it commutes with differentiation, one can use integration by parts to reduce terms with $\delta(w'')$ into terms with $\delta(w')$ and $\delta(w)$. Assembling all the terms, the expression of the Extended Hamilton's Principle for a composite piezoceramic beam will contain two governing equations,

$$-\rho A(\ddot{w} + \ddot{z}) - (YIw'')'' + (\frac{Qe_{31}V}{t_p})'' = 0 \tag{3.7}$$

$$\int_0^L \frac{Qe_{31}}{t_p} w'' dx_1 + \int_0^L \frac{2A_p\varepsilon_{33}^S}{t_p^2} V dx_1 - 2q = 0 \tag{3.8}$$

subject to variational boundary conditions,

$$M(x_1)\delta(w')\Big|_0^L = 0 \tag{3.9}$$

$$S(x_1)\delta(w)\Big|_0^L = 0 \tag{3.10}$$

Here, equation 3.7 is known as the actuator equation in its strong form, and equation 3.8 is known as the sensor equation. $M(x_1)$ is the bending moment, and $S(x_1)$ is the shear force. Equation 3.9 states that the moment at the tip of the composite piezoceramic beam is zero, and the slope at the root is zero. Equation 3.10 states that the shear force at the tip is zero, and the deflection at the root is zero.

3.2.2 Modal Analysis of Forced Response

The solution of equation 3.7 and 3.8 can be approximated by modal approximation

$$w(t,x) = \sum_{i=1}^{n} \psi_i(x) u_i(t) \tag{3.11}$$

where $\psi_i(x)$ and $u_i(t)$ are the eigenfunction and the modal coordinate of the composite piezoceramic beam for the i^{th} mode. Using the wave equation of a Euler-Bernoulli beam subjected to boundary conditions 3.9 and 3.10, the mass-normalized eigenfunction and eigenvalue of the i^{th} mode can be adopted from various dynamics and vibration texts [39, 40]. The strong form of the actuator equation 3.7 is multiplied by an arbitrary spatial eigenfunction then subsequently integrated by parts to form the weak form of the actuator equation:

$$\int_0^L \rho A(\ddot{w} + \ddot{z})\psi dx_1 + \int_0^L YIw''\psi'' dx_1 = \int_0^L \frac{Qe_{31}}{t_p}\psi'' dx_1 V \tag{3.12}$$

Substituting equation 3.11 into equation 3.12, the decoupled actuator equation becomes

$$\ddot{u}_i + k_{ij} u_i = b_i V - E_i \ddot{z} \tag{3.13}$$

where

$$k_{ij} = \int_0^L YI\psi_i''\psi_j'' dx_1 = \omega_{i,n}^2 \tag{3.14}$$

$$b_i = \int_0^L \frac{Qe_{31}}{t_p}\psi_i'' dx_1 \tag{3.15}$$

$$E_i = \int_0^L \rho A \psi_i dx_1 \tag{3.16}$$

where $\omega_{i,n}$ is the natural frequency at the i^{th} mode. Substituting equation 3.11, and $V = -R\frac{\partial q}{\partial t}$ into equation 3.8, the sensor equation becomes

$$b_i \dot{u}_j + C\dot{V} + DV = 0 \tag{3.17}$$

where

$$C = \frac{2A_p \varepsilon_{33}^S}{t_p^2} L \tag{3.18}$$

$$D = \frac{2}{R} \tag{3.19}$$

3.2.3 Multi Mode Approximation at Steady State Vibration

The decoupled actuator equation 3.13 and sensor equation 3.17 describes the steady-state voltage response and vibration response at any arbitrary excitation frequency ω. For a harmonic base excitation, let

$$z(t) = z_m e^{j\omega t} \tag{3.20}$$

$$u_i(t) = u_{complex,i} e^{j\omega t} \tag{3.21}$$

$$V(t) = V_{complex} e^{j\omega t} \tag{3.22}$$

Adding a damping component, $2\xi_i\omega_{n,i}$ to account for viscous air damping and strain-rate damping, and substituting equation 3.20, 3.21, and 3.22 into equation 3.13 and 3.17, the following matrix is obtained:

$$\left[\begin{array}{ccc|c} \ddots & & & -b_1 \\ & (\omega_{n,i}^2 - \omega^2) + 2\xi_i\omega_{n,i}j\omega & & \vdots \\ & & \ddots & -b_n \\ \hline -b_1 j\omega & \cdots & -b_n j\omega & -(C\omega j + D) \end{array}\right] \begin{bmatrix} u_{complex,1} \\ \vdots \\ u_{complex,n} \\ V_{complex} \end{bmatrix} = \begin{bmatrix} E_1 \\ \vdots \\ E_n \\ 0 \end{bmatrix} \omega^2 z_m \tag{3.23}$$

or simply

$$\begin{bmatrix} \underset{\approx}{\boldsymbol{P}} & -\underset{\sim}{\boldsymbol{b}} \\ -\omega j \underset{\sim}{\boldsymbol{b}}^T & Q \end{bmatrix} \begin{bmatrix} \underset{\sim}{\boldsymbol{u}}_{complex} \\ V_{complex} \end{bmatrix} = \begin{bmatrix} \underset{\sim}{\boldsymbol{E}} \\ 0 \end{bmatrix} \omega^2 z_m \tag{3.24}$$

The matrix above shows the decoupling of i^{th} from each other in the actuator equation, but is coupled with the sensor equation. The matrix 3.24 can be expanded to obtain the following frequency response functions (FRF):

$$\frac{V_{complex}}{z_m} = (-\omega j \underset{\sim}{\boldsymbol{b}}^T \underset{\approx}{\boldsymbol{P}}^{-1} \underset{\sim}{\boldsymbol{b}} + Q)^{-1} (\omega j \underset{\sim}{\boldsymbol{b}}^T \underset{\approx}{\boldsymbol{P}}^{-1} \underset{\sim}{\boldsymbol{E}} \omega^2) \tag{3.25}$$

$$\frac{u_{complex}}{z_m} = (\underset{\approx}{\boldsymbol{P}}^{-1}\underset{\sim}{\boldsymbol{b}})(-\omega j\underset{\sim}{\boldsymbol{b}}^T\underset{\approx}{\boldsymbol{P}}^{-1}\underset{\sim}{\boldsymbol{b}} + Q)^{-1}(\omega j\underset{\sim}{\boldsymbol{b}}^T\underset{\approx}{\boldsymbol{P}}^{-1}\underset{\sim}{\boldsymbol{E}}\omega^2) + \underset{\approx}{\boldsymbol{P}}^{-1}\underset{\sim}{\boldsymbol{E}}\omega^2 \tag{3.26}$$

FRF 3.25 is the voltage output to base displacement ratio, and FRF 3.26 is the modal displacement to base displacement ratio. To convert to physical coordinates, one can use equation 3.11.

3.3 Validation of Model

3.3.1 Comparison of Linear Bimorph Model with Literature

The piezoelectric response predicted by the model derived in previous section was compared with a linear piezoelectric model and experiment derived and conducted by Stanton [65]. Stanton also modeled the linear bimorph cantilever using first-principles energy methods. He used a bimorph cantilever (T226-H4-203X, Piezo Systems Inc.) and investigated the nonlinear effects when the bimorph cantilever was subjected to large amplitude ($2g$). However, to comply with the small displacement assumption, only results generated from low amplitude ($60mg$) excitation was used for comparison. The geometric and material properties of the composite pizeoceramic bimorph is summarized in Table 3.1. The resistor load used was $100k\Omega$.

Table 3.1: Geometric and material properties of PZT-5H bimorph cantilever[65]

Parameter	Piezoceramic (PZT-5H)	Substructure (Brass)
Length, l (mm)	24.06	24.06
Width, b (mm)	6.4	6.4
Thickness t_p, t_e (mm)	0.265	0.140
Mass density ρ_p, ρ_e (kg/m^3)	7500	9000
Elastic modulus Y_p, Y_e (GPa)	60.6	105
Piezoelectric constant e_{31} (C/m^2)	-16.6	...
Permittivity constant ε_{33}^S (nF/m)	25.55	...

The bimorph cantilever considered by Stanton is also geometrically uniform, with the exception that the bimorph configuration are in series connection, rather than in parallel connection as shown in Figure 3.2. Erturk [39] has shown that in both series connection and parallel connection, the vibration response is identical for extreme conditions of the external load resistance (short-circuit and open-circuit). At maximum or optimal power output conditions, the series connection configuration produces a larger voltage output, whereas the parallel connection configuration produces a larger current output. An example in [39] shows that to generate the same maximum power output of 0.23 mW/g^2, the series connection configuration generates a voltage amplitude of 2.8 V/g whereas the parallel connection configuration generates a voltage amplitude of 1.4 V/g, which is approximately half that of the former. Erturk also suggested that since the current output in the series connection configuration is small, the duration of charging a battery can be substantially long; and that a parallel connection configuration is preferred. Since this application is for use of harvesting energy to power electronics for use of SHM, the parallel connection configuration is preferred. However, to validate the model against Stanton's work, modifications were made to the potential difference equation. Here, $\phi^- = -V/2$ and $\phi^+ = V/2$, causing the governing equations 3.7 and 3.8 to be modified respectively as followed:

$$-\rho A(\ddot{w}+\ddot{z}) - (YIw'')'' + (\frac{Qe_{31}V}{2t_p})'' = 0 \tag{3.27}$$

$$\int_0^L \frac{Qe_{31}}{2t_p} w'' dx_1 + \int_0^L \frac{A_p\varepsilon_{33}^S}{2t_p^2} V dx_1 - q = 0 \tag{3.28}$$

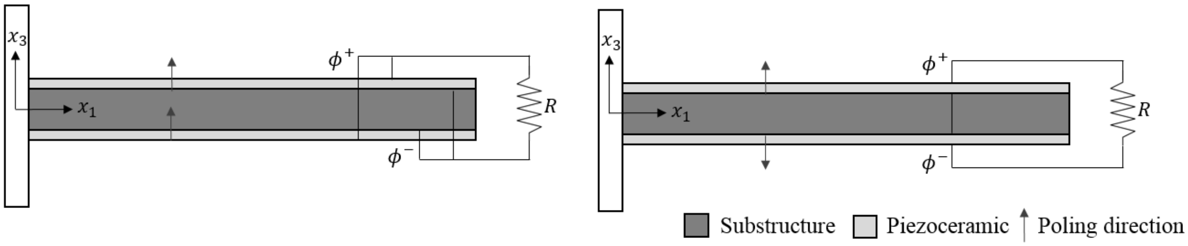

Figure 3.2: Bimorph cantilever beam in parallel connection (Left) and in series connection (Right)

Figure 3.3 shows the steady state displacement response and steady state voltage output response at ($60mg$) excitation for the model derived in this work (parallel and series), in comparison with work done by Stanton. For the parallel connection case, 0.25%, 0.75%, and 1.25% damping factor is used to predict the steady state responses since no quantitative priori knowledge of damping is known. If $\xi = 1.25\%$ is used, the amplitude of tip displacement seems to match comparably well with Stanton's work, whereas the amplitude of voltage output is lower than that that shown by Stanton. However, for the series connection case, a damping factor of 0.60% successfully predicted the steady state solution to be comparable with Stanton's work.

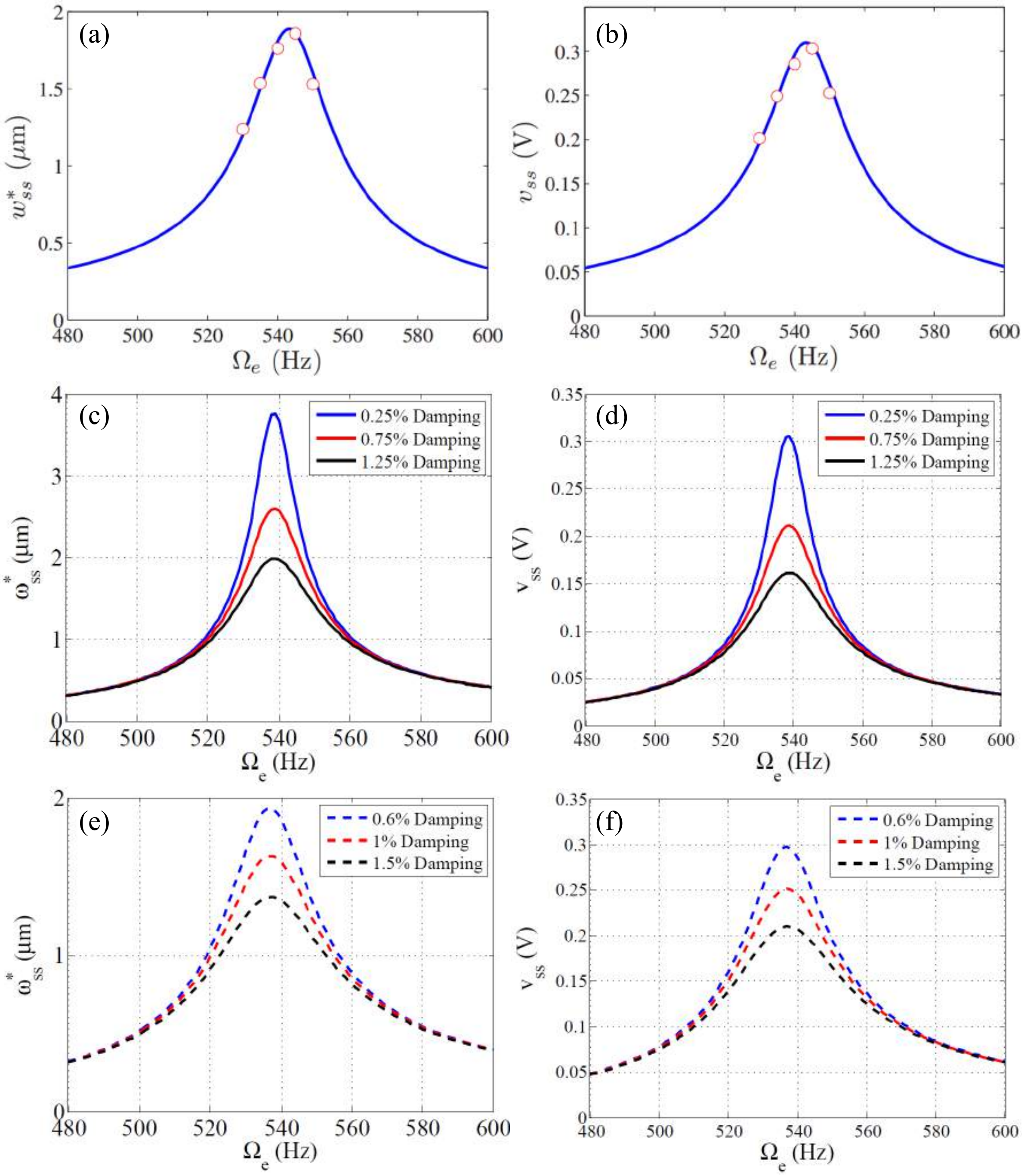

Figure 3.3: Comparable agreement between current model derived and Stanton's work in [65]. Left: Tip Displacement Frequency Response Function; Right: Voltage Output Frequency Response Function (a)-(b) Stanton's Work, blue line denotes model, red dots denote experimental results; (c)-(d) Current Model (Parallel Configuration); (e)-(f) Current Model (Series Configuration)

3.3.2 Comparison of Linear Unimorph Model with Experiment

The simulations in the previous section were conducted for a single resistance load case. To test the model's voltage output at extreme conditions (short-circuit and open-circuit), a commercially available piezoelectric patch was purchased and tested. A QuickPack-1001 (Figure 2.1 was purchased from Mide Technology and clamped in a cantilever beam configuration. A thorough explanation on the experimental setup can be found in section 4.2.1. The resistance loads were varied from 1Ω to $10M\Omega$. The cantilever piezoelectric QuickPack was excited at its first resonant frequency (172 Hz at $10k\Omega$ load) at different amplitudes. The voltage output was measured, and its power output calculated. It is noted that the voltage output increases monotonically, and consists of linear asymptote at extreme load conditions (short-circuit and open-circuit). It should be noted that the short-circuit voltage asymptote varies linearly with resistive load, but the open-circuit voltage asymptote is not dependant on it [39]. The power plot suggests that there exists an optimum resistive load for maximum power generation.

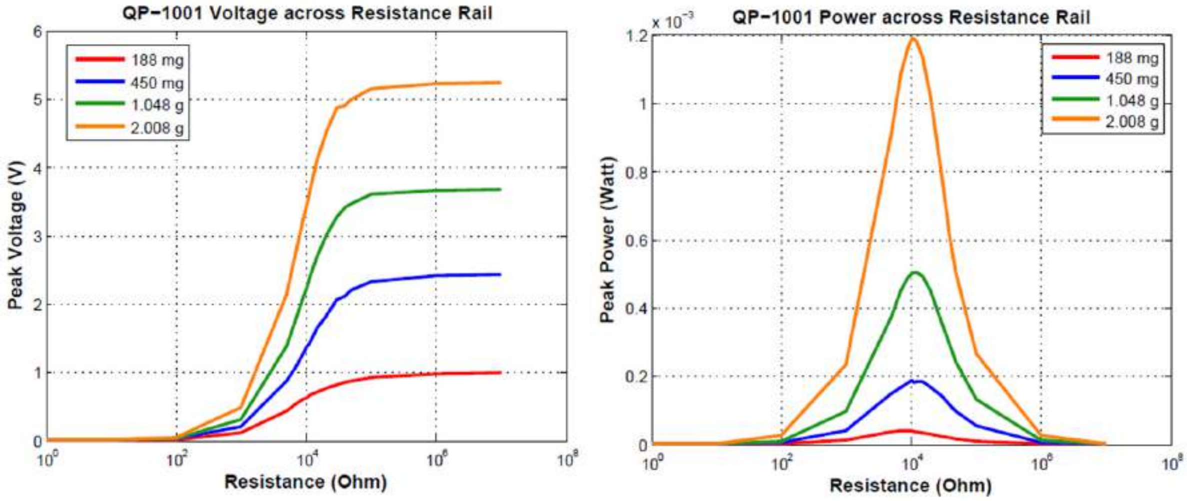

Figure 3.4: Experimental characterization of QuickPack 1001; Left: Voltage output vs. resistive load; Right: Power output vs. resistive load

The model was reduced to a unimorph configuration to better reflect the composite setup of the QuickPack. The geometric parameters were estimated and tuned via trial and error. The piezoelectric constant and permittivity constant were estimated by using the values of PZT-5H and PZT-5A as a starting guessing point. The values are tabulated in Table 3.2. The same resistive loads were varied and simulated for the unimorph model case. The same behavior of linear asympote at extreme load conditions for voltage output and a maximum power generation between the extreme load conditions is observed. It should be noted that there exist a rightward shift of optimal resistive load when mechanical damping is reduced. This can be attributed to the fact that the short-circuit resonant frequency does not depend on mechanical damping, but the open-circuit resonant frequency does depend on mechanical damping [39].

Table 3.2: Piezoelectric properties

	e_{31} (C/m^2)	ε_{33}^S (nF/m)
PZT-5H	-16.60	25.55
PZT-5A	-10.40	13.30
QuickPack	-11.58	12.58

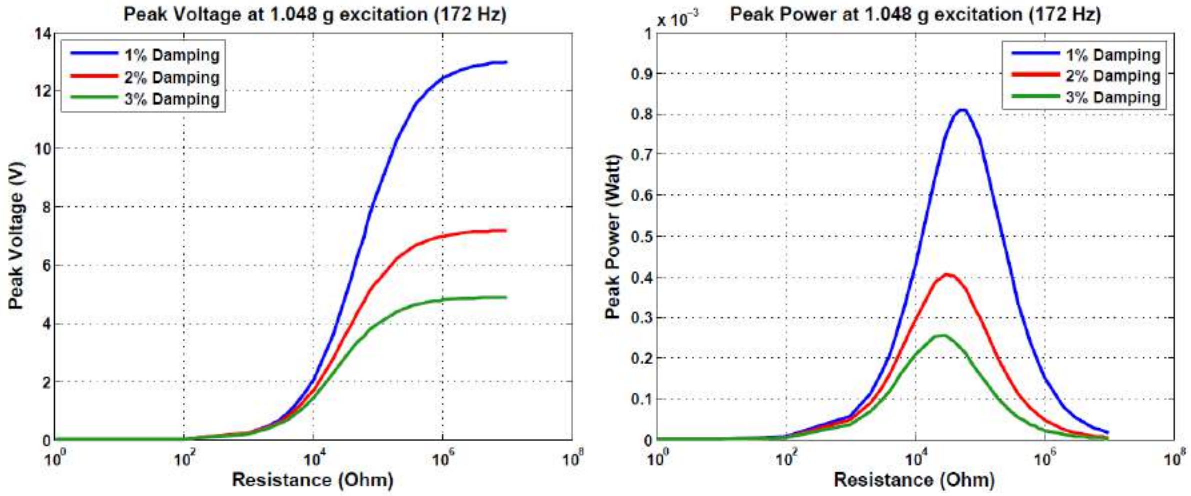

Figure 3.5: Unimorph Model with approximate parameters; Left: Voltage output vs. resistive load; Right: Power output vs. resistive load

The results from this section shows the voltage and power output behavior as a function of resistive load. The following section will characterize the power generation capability of a novel piezoelectric nanostructure by the investigation of its voltage and power output vs. resistive load.

Chapter 4

Experimental Characterization of Piezoelectric ZnO Nanowires

4.1 Fabrication of Carbon Fiber Reinforced Polymer Composites with Embedded ZnO Nanowires

Plain-woven glass fiber (GF) fabric was used for primary reinforcements. A thin layer (75 nm) of amorphous ZnO was sputtered on both sides of the glass fiber fabric using a OTC Orion high vacuum magnetron sputter system manufactured by AJA International Inc. The sputtering process was conducted under 3 mTorr inert argon atmosphere and using a 300 Watts RF power. The pre-coating of amorphous ZnO layer provides initiation seeds for growing ZnO nanowires on the glass fiber. The use of magnetron sputtering system with accuracy of atomic layer aids in the uniform coating of ZnO. However, due to the curvature of the fibers, there might be a slight variation in the thickness of ZnO amorphous layer across the glass fiber. Results so far indicate that a thicker amorphous layer yields a much larger diameter and slightly shorter nanowires. An aquatic solution of zinc acetate dihydrate (Zn(O2CCH3)22H2O) and hexamethylenetetramine (HMTA) in deionized (DI) water (30 mM each) was used to conduct a hydrothermal ZnO nanowire synthesis technique. The pre-coated fabric samples were immersed in the aquatic solution and kept inside a convection oven at 85 $^\circ C$ for 8 hours. Then, the ZnO nanowire grown fabric samples were rinsed with DI water and kept to dry overnight inside the oven.

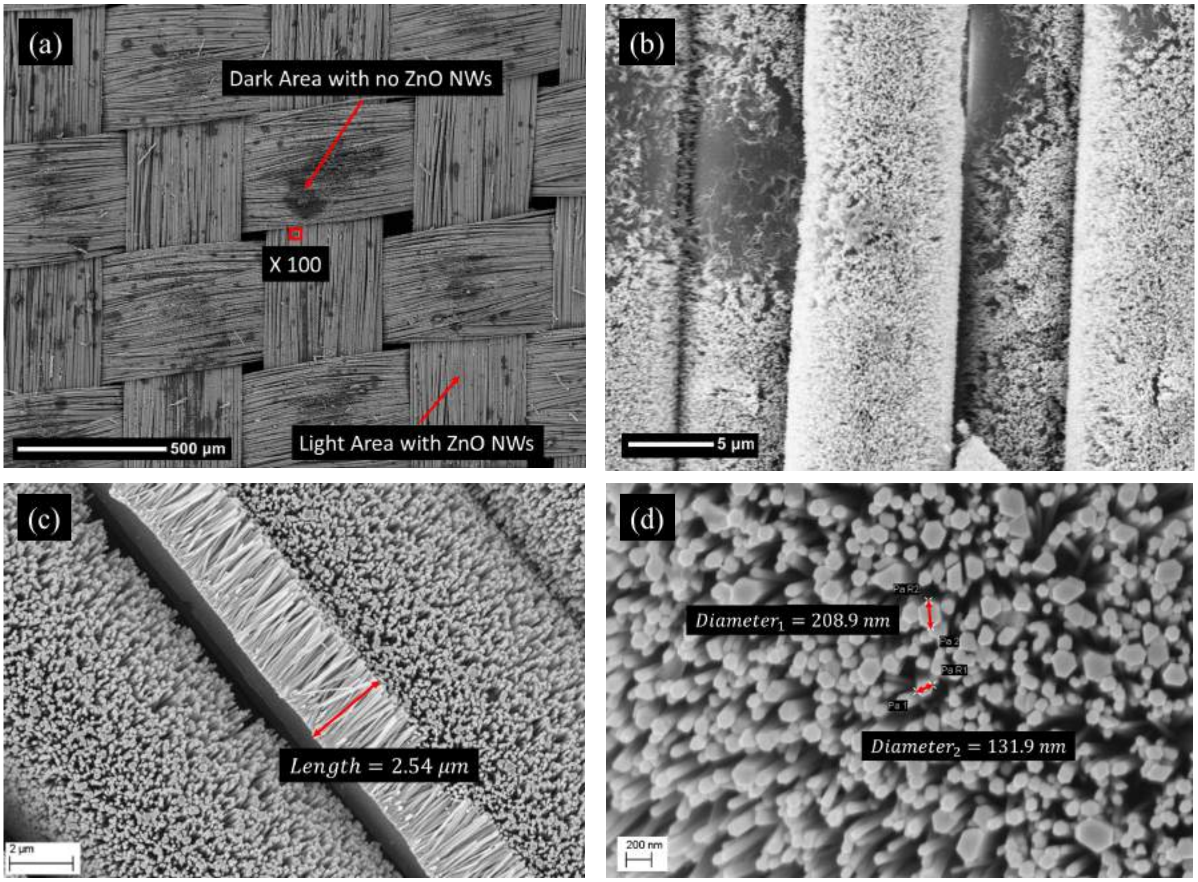

Figure 4.1: Scanning Electron Microscope micrograph of glass fiber grafted with ZnO nanowires; Top photos taken with NeoScope JCM-5000 Benchtop operating at 15kV, bottom photos taken with 5300 Hitachi FE-SEM Electron Microscope operating at 5 kV; (a) 100 μm, (b), (c) 1 μm, (d) 100 nm

The carbon fiber reinforced polymer laminates were fabricated using a vacuum- and pressure-assisted hand layup system. Aeropoxy^{TM} manufactured by PTM&W Industried Inc. was used as the polymer matrix. Plain-woven carbon fiber (CF) fabrics were used as top and bottom layers of the final laminates, and serve as electrodes. Considering the work function of the carbon fiber and electron affinity of the ZnO nanowires, an Ohmic contact rather than a rectified Schottky barrier behavior is anticipated. The fabricated composite beam samples possessed the following stacking sequence: CF/ZnO grafted GF/ZnO grafted GF/CF.

4.2 Experimental Investigation of Energy Harvesting Capabilities

4.2.1 Experimental Setup

The composite beam samples were fixed to a vibration shaker in a cantilevered configuration. Leads were attached on the CF fabric on both sides of the samples, and were connected in series to a resistance decade box. The base of the beam samples was excited under controlled vibratory excitations using a LDS V408 vibration shaker with a PA100E power amplifier. A Polytec laser vibrometer was used to measure the tip velocity of the beam, and a PCB triaxial accelerometer (Model 354C03, 100 mV/g) was used to measure the base acceleration. A National Instruments system with a PXI-4461 (24-Bit, 204.8 kS/s, 2-Input/2-Output), a PXI-4462 (24-Bit, 204.8 kS/s 4-Input), and a NI PXI-4071 7.5 digit digital multimeter were used to record the tip velocity, base acceleration, and voltage output from the composite beam sample. The digital multimeter has a precision of 10 nV. Assuming negligible power dissipation in the wires, and ignoring mechanical damping, the potential difference measured across the resistance connected in series with the composite beam sample was used to quantify power dissipation. Voltage was measured at a sampling frequency of 20 kHz.

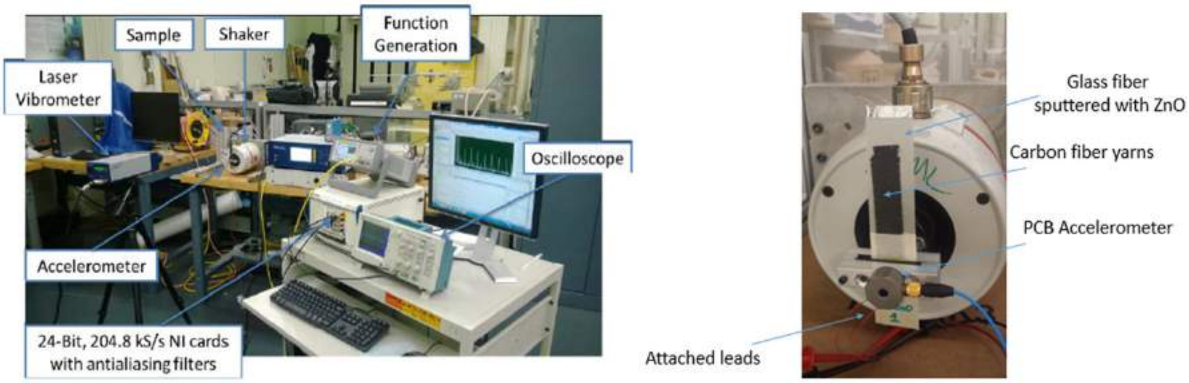

Figure 4.2: Experimental setup for energy harvesting tests

Due to low voltage signals from the composite beam samples, environmental pick-ups from power cords, computer monitors, and fluorescent lighting could become sources of noise in the data acquisition setup. Significant efforts were conducted in the identification and isolation of noise. A Faraday shield was constructed from 80 x 80 mesh size stainless steel woven wire cloth with an opening size of 0.006". The effectiveness of the Faraday shield was demonstrated by the reduction of 60 Hz noise by 50 dB. To investigate the effect of the shaker on noise level, the composite beam sample was connected to the circuit and placed next to the shaker. The voltage output from the sample was recorded with the shaker driven at 30

Hz sine wave. The voltage measured from the composite beam sample was approximately an order of magnitude smaller than the noise level generated by the 60 Hz electrical noise. The noise from generated from the shaker is considered as negligible.

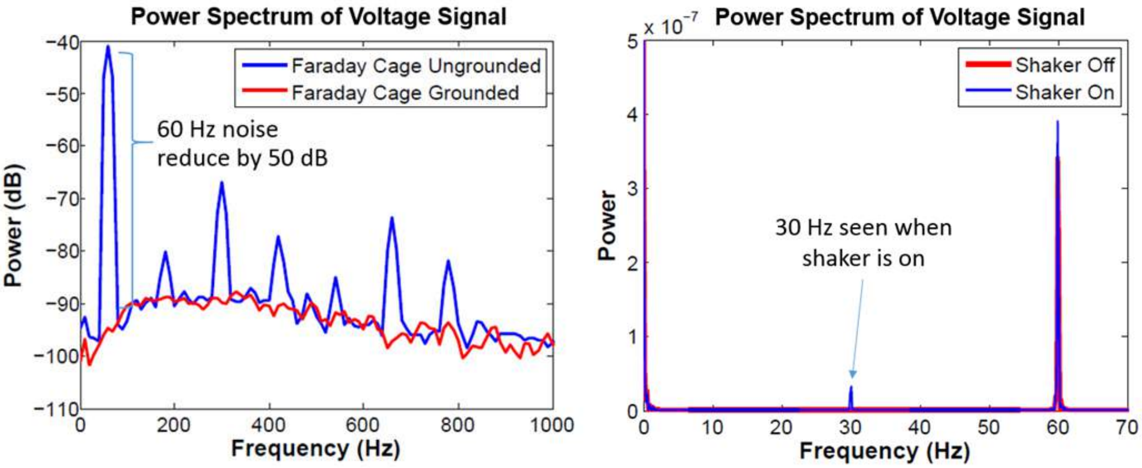

Figure 4.3: Left: Power spectrum with and without grounded Faraday shield; Right: Power spectrum of voltage output signal with and without shaker on.

4.2.2 Results

White noise was used to excite the base of the cantilever composite beam sample. The frequency response function (FRF) of voltage response was obtained for each composite beam samples and its natural frequency identified (See Figure 4.4). The peak voltage was collected for a range of known impedance loads with values between 1 kΩ and 10 MΩ. It was demonstrated that as voltage increases, the voltage output FRF shifts upwards, showing an increase in voltage output.

The subsequent tests were done by exciting the cantilever composite beam sample with a sine wave at its first natural frequency. This was done because the maximum output voltage was observed at its first natural frequency (See Figure 4.4). To demonstrate the piezoelectric coupling of ZnO nanowires, a reference sample without ZnO nanowires was fabricated and tested. The composite beam samples were excited at two levels of 1.7g and 2.6g to demonstrate the proportionate increase in peak voltage (See Figure 4.5). The peak power generated by the sample was calculated using the power formula:

$$P_{peak} = \frac{V_{peak}^2}{R} \tag{4.1}$$

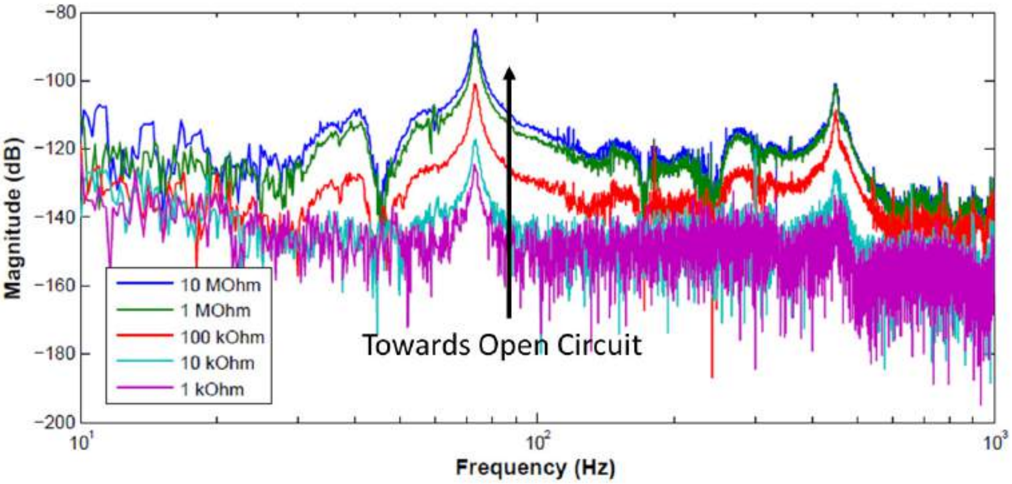

Figure 4.4: Typical frequency response function of voltage response. Input - Base Excitation, Output - Voltage Response.

A maximum of 6.7 mV was obtained when the composite beam sample with ZnO nanowires was excited at 2.90g and connected to 10 MΩ. Results comparing the cantilever composite beam with and without ZnO nanowires show that the voltage generated was indeed due to the piezoelectric effects of the ZnO nanowires. The calculated power was also plotted against the known resistance value to determine the approximate resistance value where optimal power is generated. The maximum power occurs at a resistance value of approximately 1 MΩ, which is relatively close to the measured impedance of the sample (1.56 MΩ). The maximum peak power generated by the composite beam sample at this resistance was calculated to be 20.0 pW.

To increase deflection of the composite beam sample, a 0.6 gram tip mass was added to the beam, whilst maintaining the same base excitation level. Tests show that an increased deflection of the composite beam sample yielded an increase of 2.21 mV when connected to a resistor of 10 MΩ, and an increase of 13.3 pW when connected to an optimal resistor of 1 MΩ.

A series of DC voltages was applied across a new composite beam sample with ZnO nanowires to see if it has the same effect as poling treatment typically performed on piezoceramic sensors. A shift in voltage and power generation may be an indication of dipole realignment in the piezoelectric material. First, a 10 V DC was applied for 60 seconds. An increase in peak-power was observed. Then a 20V DC was applied on the same sample for 60 seconds. A decrease in peak-power was observed. The reduction in power after the application of 20 V DC can be result of exposure to the high electrical field since the nanowires are only several microns in length.

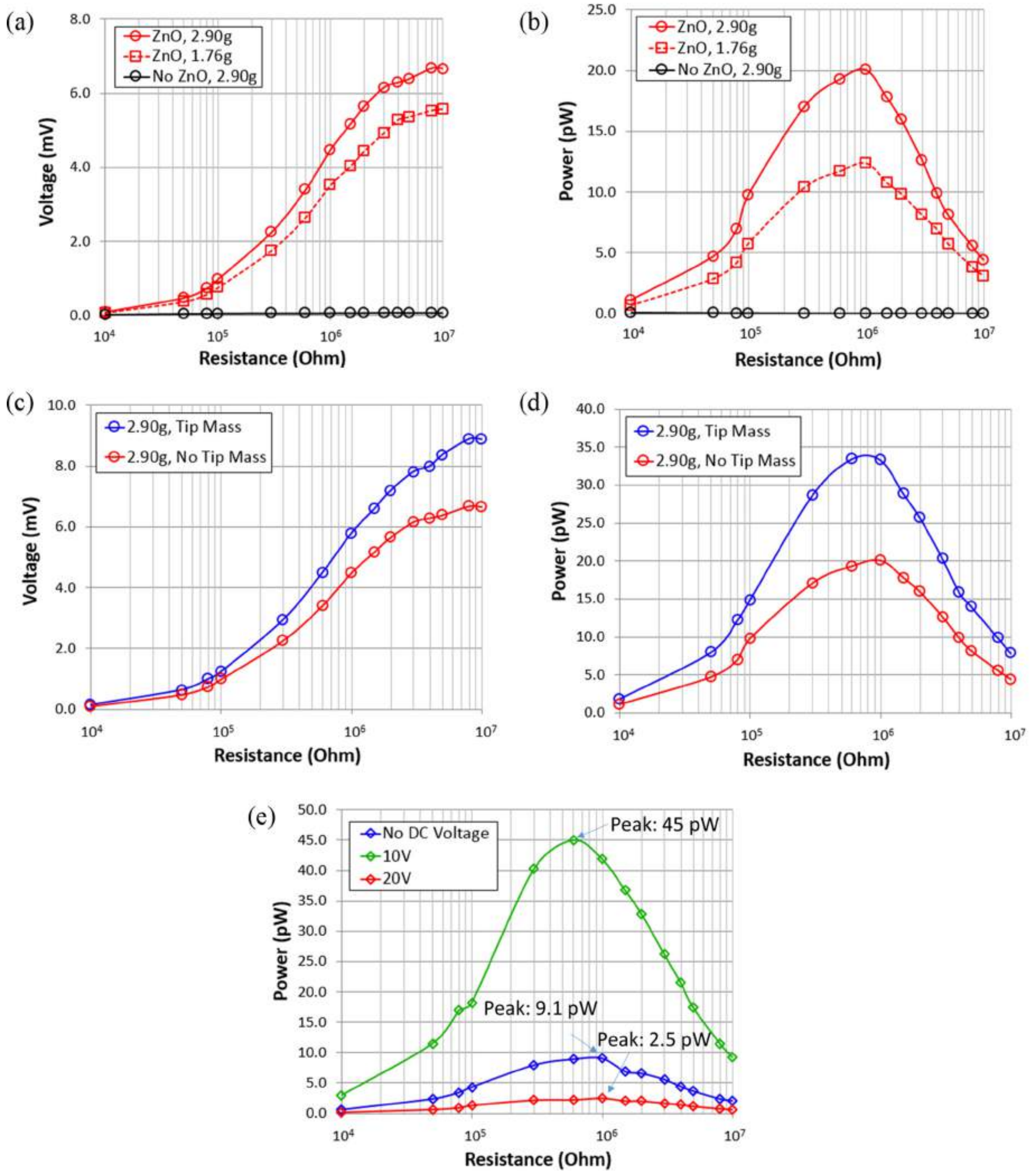

Figure 4.5: Voltage and power generated across resistance rail; (a)-(b) Comparison of composite beam samples with and without ZnO NWs and at different excitation level; (c)-(d) Comparison of composite beam samples with and without tip mass (e) Effect of application of DC voltage

To investigate the possible scale up of energy harvesting capabilities, tests were conducted on increased number of glass fiber layers and increased width of the cantilever composite beam. Three baseline composite beam samples with each side of two glass fibers and the inner side of CF layer were sputtered with ZnO amorphous layer. The fabrication process was the same as described in Section 4.1. Two composite beam samples with twice the number of glass fiber layer (with ZnO nanowire), one composite beam sample with twice the width, and one composite beam sample with three times the width were fabricated. All samples have identical length. Testing procedure were identical as previous tests, with excitation level maintained at 1.0g for all cases. Results show that doubling the glass fiber layers with ZnO nanowires increased the maximum power output by 0.8 pW. However, doubling and tripling the width of the cantilever beam decreases the power output. It should be noted that all samples were excited at 1.0g amplitude but at their respective fundamental frequency. The reduction in power output could be due to the increased damping in the mechanical response or the decreased deflection from increased width.

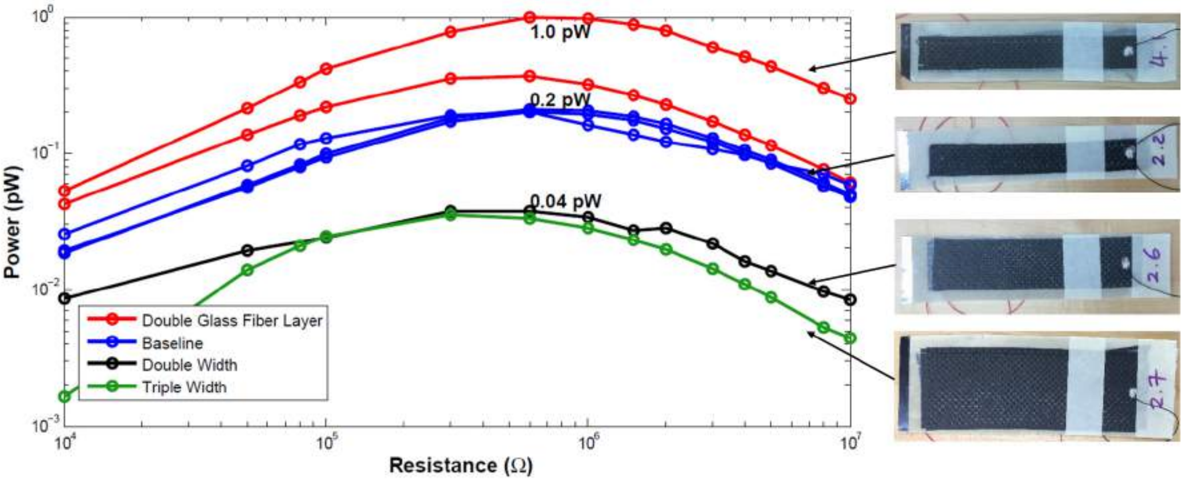

Figure 4.6: Peak power at constant excitation level 1.0g for composite beam sample with different layup sequence, or different width.

Effort was also conducted to correlate power generated to axial strain at the root of the composite beam sample. The steady state tip displacement response from the analytical model derived in Section 3.2 was matched with the experimental tip displacement responses at original length and reduced length of the composite beam sample. The maximum axial strain at the root was calculated using the following equation:

$$S_{11,ss} = -x_3 \frac{\partial^2 w_{ss}}{\partial x_1^2} \tag{4.2}$$

The power generated was normalized by 1% maximum strain (See Figure 4.7). It was observed that the composite beam sample with larger length yields a maximum peak power of 10.64 pW per 1% strain as compared to the 5.4 pW per 1% strain yielded by the shorter composite beam sample.

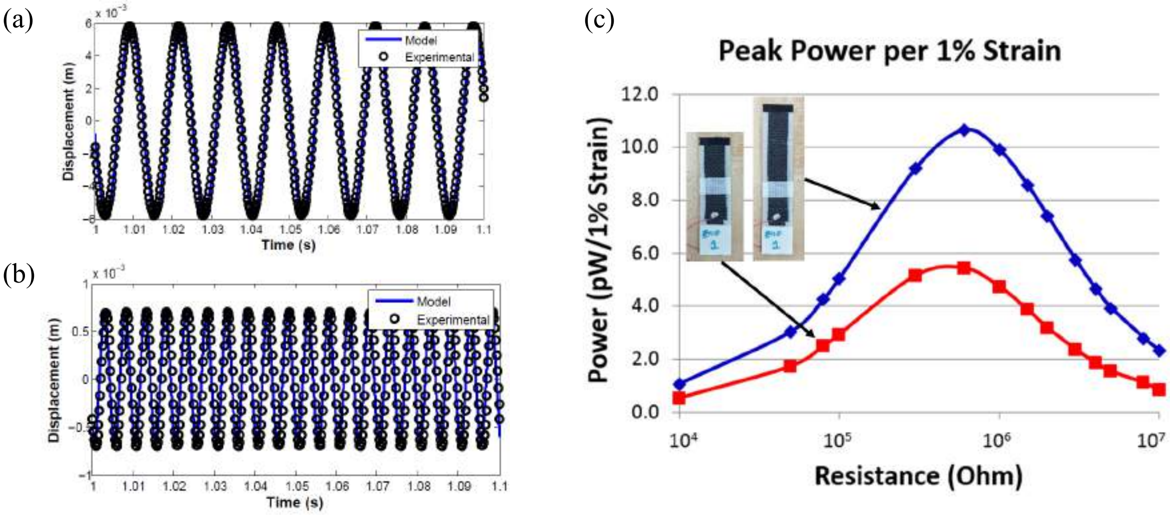

Figure 4.7: (a)-(b) Steady state tip displacement response; Original length excited at 79 Hz; Reduced length excited at 200 Hz. (c) Strain normalized peak power

4.3 Modelling of Composite Piezoelectric Beam with Properties of ZnO Nanowires

As described in Section 2.1, equation 2.1 shows the linear constitutive relation for piezoelectric materials. From a materials perspective, the energy harvesting capability of a piezoelectric bimorph is a function of the plane stress piezoelectric constant, e_{31}, and its permittivity constant ε_{33}^{S}. A commonly used term to characterize the permittivity constant is the dielectric constant ε_r, where the electric permittivity of any medium can be compared relative to the permittivity of free space $\varepsilon_0 = 8.854 \times 10^{-12} F/m$ by the equation

$$\varepsilon = \varepsilon_r \varepsilon_0 \tag{4.3}$$

Previous research [66, 67] has sucessfully shown the size dependence of the piezoelectric properties in a single ZnO nanowire. Figure 4.8 shows their dependence as a function of nanowire diameter. Referring to Figure 4.1, the ZnO nanowires grown in this work have an estimated diameter of $200nm$, and length of $2.54\mu m$. Investigating Figure 4.8, the e_{31} value must be between $-0.15C/m^2$ and $-0.63C/m^2$, and the dielectric constant is approximately 4.5

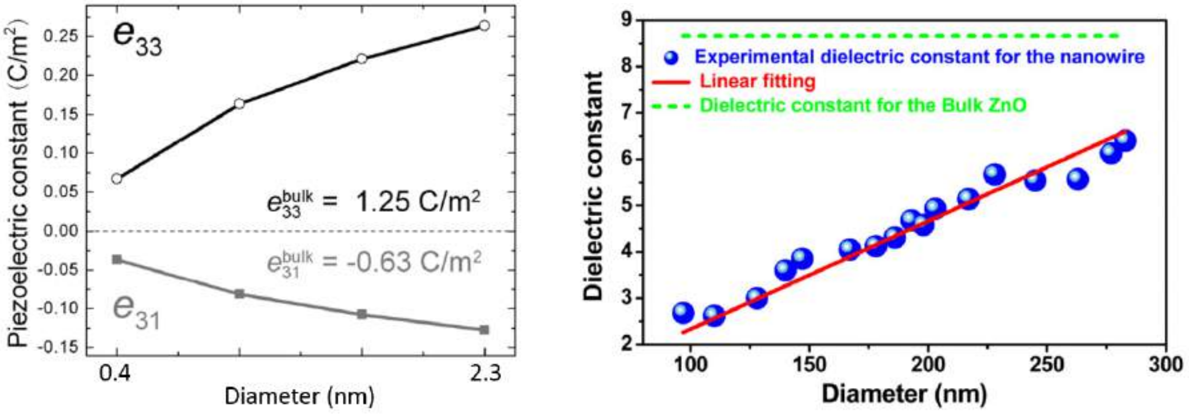

Figure 4.8: Left: Effective piezoelectric constants of ZnO nanowires [66], Right: Diameter dependence of dielectric constant in a single pencil-like ZnO nanowire [67]

Using the extrapolated e_{31}, the interpolated ε_{33}^{S}, and the length of the ZnO nanowire as the thickness of piezoelectric material, the model derived in Section 3.2 was used to predict the expected voltage output. Here, the geometric properties which govern the dynamics of a cantilever beam (thickness, density, young's modulus, length) was measured and fine-tuned so the natural frequencies predicted by the model matches the ones measured in experiment. The parameters are listed in Table 4.1. A series of frequency response functions were plotted by changing the resistive load. Experimentally, the composite beam with piezoelectric ZnO nanowires were excited with white noise (setup described in Section 4.2.1), and its voltage output frequency response function obtained by fast fourier transform.

Table 4.1: Geometric and material properties used for model

Parameter	Composite Beam
Length, (mm)	77.3
Width, (mm)	26.64
Effective thickness, (mm)	0.71
Mass density (kg/m^3)	961.1
Elastic modulus (GPa)	14
Active layer thickness (μm)	2.6
Piezoelectric constant (C/m^2)	-0.3
Dielectric constant	4.5

Figure 4.9 shows the voltage output frequency response function obtained experimentally and theoretically. A quick observation shows the increase in voltage output towards an asymptote at high resistive load (open-circuit condition) as described in previous sections.

However, observing the maximum voltage output at the first mode, the model overpredicts voltage output by $52dB$. That corresponds to about 300 times the amplitude of voltage output produced experimentally. The discrepancy in voltage output prediction is most likely due to the simplified assumptions in the model, which failed to account for the following: (i) Non-uniform length, diameter and volume fraction of NWs, (ii) Radially grown NWs on the host fibers, (iii) Non-uniform poling direction and conductibility of NWs with the host fibers. Also, since the piezoelectric constant and dielectric constant is strongly dependant on stress and temperature, it is uncertain whether the piezoelectric properties obtained in Figure 4.8 corresponds to the properties of the NWs in this work. These factors could serve as a starting point for future research, and if treated, it indicates the potential high voltage output. It also provides a good reference in the field of embedding ZnO NWs for energy-harvesting purposes.

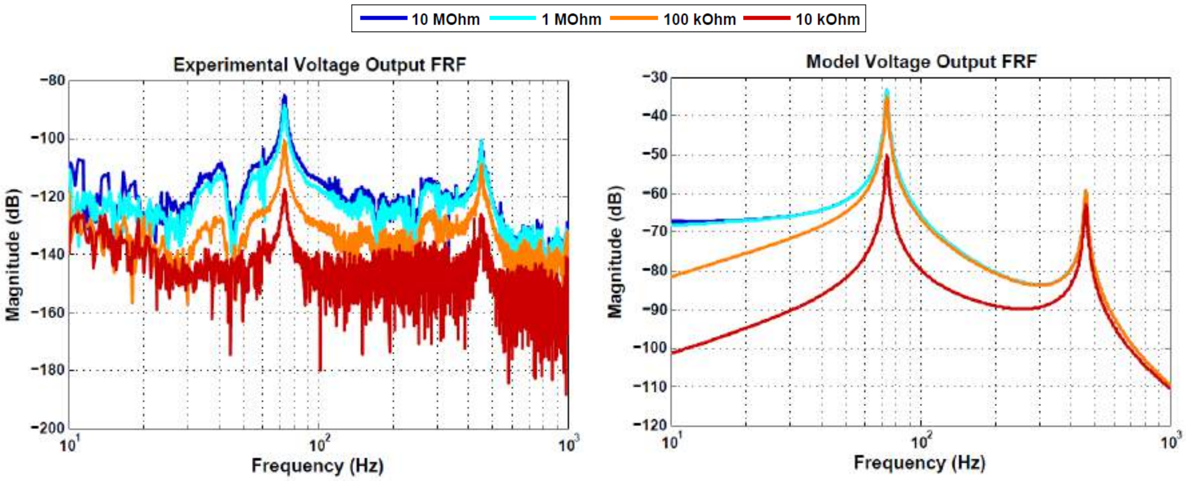

Figure 4.9: Left: Voltage Frequency Response Function obtained Experimentally; Right: Voltage Frequency Response Function obtained Theoretically

Chapter 5

Conclusion

5.1 Summary of Work

In this work, the concept of a self-powered SHM smart tire was demonstrated using piezoelectric materials. It was shown that with commercially available piezoelectric patches such as QuickPack and Macro Fiber Composite, impedance-based SHM could be applied on an aluminum beam and on a tire section. Three tests were conducted in the SHM portion of this work - Beam with QuickPack, Beam with MFC, and Tire Section with MFC. The first test showed that two QuickPack sensors can be connected in parallel to conduct impedance-based SHM on a beam. This suggests the possibility of connecting several sensors in parallel or in series for large structures such as a tire, to significantly reduce interrogation time. However, damage detection sensitivty and damage localization was reduced. The second test successfully demonstrated the use of a modified I-V probe circuit as a high voltage impedance analyzer for use of impedance-based SHM. However, this introduces two additional variables - voltage and resistance that needs to be tuned according to the application. The test demonstrated that higher frequency ranges are more favorable for damage detection due to the vast amount of resonant peaks in the electrical impedance signature. The test also suggests the ability of a high voltage impedance analyzer to provide insight on damage type and damage location. The final test shows the use of the technique on a tire section. However, its capability was severely reduced due to the attenuation of resonant peaks in the electrical impedance signatures, as a result of the low stiffness and high damping characteristics of the material. A clamp was applied on the tire section, and the shift in electrical impedance signature was shown by the E4990A impedance analyzer. The damage identification for the tire section was enhanced by the addition of resistor-capacitor-inductor circuits. Two tests involving one set of RCL circuit and four sets of RCL circuits were conducted. The test with four sets of RCL circuits successfully detected the presence of belt separation. The damage metric for the test with four RCL circuits were significantly higher than the test with one RCL circuits, suggesting the need to increase the number of electrical circuits needed to enhance damage identification.

Chapter 3 shows that a bimorph piezoelectric energy harvester model can be derived using the extended Hamilton's principle and the linear constitutive relations of piezoelectric materials. However, this limites the simulation for low excitation levels where the Euler-Bernoulli assumption will not be void. Modal analysis was conducted for harmonic sinusoidal excitation, obtaining frequency response functions for voltage output and tip displacement. The model was validated against literature, particularly with the model prediction and experimental work done by Stanton [65]. The validation work shows a more accurate prediction when a bimorph in series connection was used. The model was reduced to a unimorph model to compare the voltage prediction at different loading conditions. Experimental work was conducted with a QuickPack sensor to validate the voltage output behavior. It was demonstrated that the voltage output increases monotonically, and consists of a linear asymptote at extreme loading conditions (short-circuit and open-circuit). It was also demonstrated that there exist an optimal resistive load for maximum power output.

For the energy harvesting portion of this work, ZnO nanowires were successfully grown on plain-woven glass fiber fabric. Plain-woven carbon fiber fabrics were used as top and bottom layers of the final laminates, and serve as electrodes. This process demonstrates the possibility of embedding ZnO nanowires in a tire, and is left for future investigation. The composite beam samples were clamped in a cantilever position and were excited at two levels - 1.7g and 2.6g. The voltage output was also shown to increase monotonically with linear asymptotes as demonstrated in Chapter 3. A maximum of 6.7 mV was obtained when the composite beam sample with ZnO nanowires was excited at 2.90g and connected to 10 $MOhm$. A maximum power of 20.0 pW occurs at a resistance value of approximately 1 $MOhm$, which is relatively close to the measured impedance of the sample (1.56 $M/Omega$). Comparison of this voltage and power output with a baseline sample without ZnO nanowires confirmed the energy harvesting capability of the active material involved. The addition of a 0.6 gram tip mass increased the maximum voltage output by 2.21 mV and the maximum power output by 13.3 pW. A series of DC voltage induced across the composite beam sample shows an increase in peak power when 10V DC was applied, but a reduction in peak power when a 20V DC was applied subsequently. Doubling the number of glass fiber layers increased the power output by 0.8 pW. However, doubling and tripling the width of the composite beam reduced the power generation. The length of a composite beam with nominal power output of 10.64 pW per percentage strain was reduced and its power output calculated. The power output reduced to 5.4 pW per percentage strain. Finally, the piezoelectric constant and dielectric constant of a single ZnO nanowire was obtained from literature and inserted in the model in Chapter 3. The theoretical voltage output frequency response function was compared with that obtained experimentally. The model overpredicts the voltage output by 52 dB at the first mode. The discrepancy is likely attributed to the non uniform length, diameter, and volume fractions of NWs in the experiment, the radially grown NWs on the host fibers, and the non-uniform poling direction and conductibility of NWS with the host fibers.

5.2 Recommendations for Future Work

Under the damage identification enhancement with electrical circuit portion of this research, a very simple resistor-capacitor-inductor circuit was used. This has room for future improvement with incorporation of more advanced circuits such as negative capacitance and negative resistance circuits. With the absence of resonant peaks in the electrical impedance signature when piezoelectric sensors were attached on the tire, this remains the most crucial study that should be investigated further.

For the energy harvesting work, the theoretical model shows a higher voltage output by 52 dB when compared to experimental work. This shows the potential of ZnO nanowires for power generation. One way to mimic the theoretical model is to grow ZnO nanowire laterally and vertically on the top and bottom surface of the glass fiber layer. Another suggestion is to increase the volume fraction of the ZnO nanowires during the fabrication process. While this work only investigated the maximum voltage and power output generated by the energy harvester, future work should investigate optimal circuits such as an AC-DC rectifier circuit for the design of an optimal ”charging station”.

Lastly, a combination of the SHM and energy harvesting work can be implemented in an outdoor ”field test” involving the attachment of commercially available piezoelectric patches on the inner surface of a tire. Work should be carried out to understand the effects of tire inflation, driving conditions, and environmental noise before a ”Smart Tire” can be realized. Figure 5.1 shows the setup available for such tests.

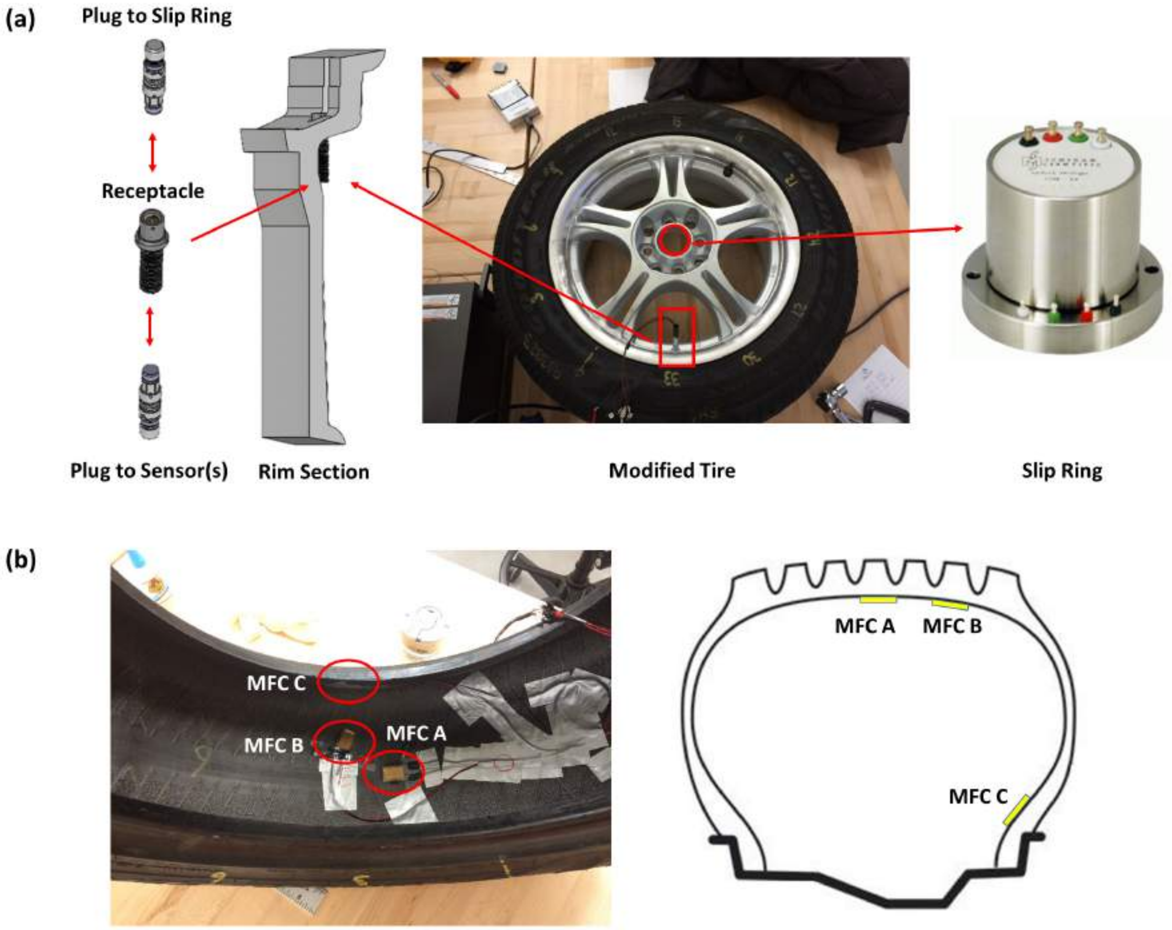

Figure 5.1: Setup for "Field Test"; (a) Exterior of tire showing connections and slip ring; (b) Interior of tire showing the attachment of MFC sensors

Bibliography

[1] Kais Mnif. A smart tire pressure monitoring system. *Sensors*, 18(11):40–46, 2001.

[2] Olivier Bellavigna Toan Vu-Khanh Patricia Dolez Carlos Arrieta Cédrick Nohilé Tung Ha-Anh René Benoît, Michel Gou. Heavy vehicles tire blowout and explosion. Technical report, Association Sectorielle Transport Entreposage, 2009.

[3] Thomas Giapponi. Tire forensic investigation. Technical report, SAE Technical Paper, 2008.

[4] Michael YY Hung, Yun Shen Chen, Siu Pang Ng, Steven M Shepard, Yulin Hou, and James R Lhota. Review and comparison of shearography and pulsed thermography for adhesive bond evaluation. *Optical engineering*, 46(5):051007–051007, 2007.

[5] Sinem Coleri Ergen, Alberto Sangiovanni-Vincentelli, Xuening Sun, Riccardo Tebano, Sayf Alalusi, Giorgio Audisio, and Marco Sabatini. The tire as an intelligent sensor. *Computer-Aided Design of Integrated Circuits and Systems, IEEE Transactions on*, 28(7):941–955, 2009.

[6] Ryosuke Matsuzaki and Akira Todoroki. Wireless monitoring of automobile tires for intelligent tires. *Sensors*, 8(12):8123–8138, 2008.

[7] Jingang Yi. A piezo-sensor-based "smart tire" system for mobile robots and vehicles. *Mechatronics, IEEE/ASME Transactions on*, 13(1):95–103, 2008.

[8] Ryosuke Matsuzaki and Akira Todoroki. Intelligent tires for improved tire safety using wireless strain measurement. In *The 15th International Symposium on: Smart Structures and Materials & Nondestructive Evaluation and Health Monitoring*, pages 69321A–69321A. International Society for Optics and Photonics, 2008.

[9] Gyuhae Park and Daniel J Inman. Structural health monitoring using piezoelectric impedance measurements. *Philosophical Transactions of the Royal Society of London A: Mathematical, Physical and Engineering Sciences*, 365(1851):373–392, 2007.

[10] Gyuhae Park, Tajana Rosing, Michael D Todd, Charles R Farrar, and William Hodgkiss. Energy harvesting for structural health monitoring sensor networks. *Journal of Infrastructure Systems*, 14(1):64–79, 2008.

[11] Hoon Sohn, Charles R Farrar, Francois M Hemez, Devin D Shunk, Daniel W Stinemates, Brett R Nadler, and Jerry J Czarnecki. *A review of structural health monitoring literature: 1996-2001.* Los Alamos National Laboratory Los Alamos, NM, 2004.

[12] Charles R Farrar and Keith Worden. Fundamental axioms of structural health monitoring. *Structural Health Monitoring: A Machine Learning Perspective*, pages 439–460, 2005.

[13] Matthew E Palmer, Clark C Boyd, Jim McManus, and Scott Meller. Wireless smart tires for road friction measurement and self state determination. In *Proc. 43rd AIAA/ASME/ASCE/AHS/ASC Structures, Structural Dynamics, and Materials Conference, AIAA*, page 1548, 2002.

[14] Joseph Davidson and Changki Mo. Recent advances in energy harvesting technologies for structural health monitoring applications. *Smart Materials Research*, 2014, 2014.

[15] Steven W Arms, CP Townsend, DL Churchill, JH Galbreath, and SW Mundell. Power management for energy harvesting wireless sensors. In *Smart Structures and Materials*, pages 267–275. International Society for Optics and Photonics, 2005.

[16] AYOUB YARI BOROUJENI, MICHAEL PHILEN, and MARWAN AL-HAIK. Smart hybrid zno nanowire/carbon fiber reinforced polymer composites with in-situ structural health monitoring capability. In *American Society of Composites-30th Technical Conference*, 2015.

[17] Renato Caliò, Udaya Bhaskar Rongala, Domenico Camboni, Mario Milazzo, Cesare Stefanini, Gianluca de Petris, and Calogero Maria Oddo. Piezoelectric energy harvesting solutions. *Sensors*, 14(3):4755–4790, 2014.

[18] A Erturk, J Hoffmann, and DJ Inman. A piezomagnetoelastic structure for broadband vibration energy harvesting. *Applied Physics Letters*, 94(25):254102, 2009.

[19] Shashank Priya and Daniel J Inman. *Energy harvesting technologies*, volume 21. Springer, 2009.

[20] Chankyu Lee, Karl Hedrick, and Kyongsu Yi. Real-time slip-based estimation of maximum tire-road friction coefficient. *Mechatronics, Ieee/Asme Transactions On*, 9(2):454–458, 2004.

[21] Jingang Yi, Luis Alvarez, and Roberto Horowitz. Adaptive emergency braking control with underestimation of friction coefficient. *Control Systems Technology, IEEE Transactions on*, 10(3):381–392, 2002.

[22] Georg F Mauer. A fuzzy logic controller for an abs braking system. *Fuzzy Systems, IEEE Transactions on*, 3(4):381–388, 1995.

[23] Fredrik Gustafsson, Markus Drevo, Urban Forssell, Mats Lofgren, Niclas Persson, and Henrik Quicklund. Virtual sensors of tire pressure and road friction. Technical report, SAE Technical Paper, 2001.

[24] Alfred Pohl, Reinhard Steindl, and Leonhard Reindl. The “intelligent tire” utilizing passive saw sensors measurement of tire friction. *Instrumentation and Measurement, IEEE Transactions on*, 48(6):1041–1046, 1999.

[25] Ryosuke Matsuzaki and Akira Todoroki. Wireless strain monitoring of tires using electrical capacitance changes with an oscillating circuit. *Sensors and Actuators A: Physical*, 119(2):323–331, 2005.

[26] Ryosuke Matsuzaki and Akira Todoroki. Wireless flexible capacitive sensor based on ultra-flexible epoxy resin for strain measurement of automobile tires. *Sensors and Actuators A: Physical*, 140(1):32–42, 2007.

[27] Ryosuke Matsuzaki, Timothy Keating, Akira Todoroki, and Naoki Hiraoka. Rubber-based strain sensor fabricated using photolithography for intelligent tires. *Sensors and Actuators A: Physical*, 148(1):1–9, 2008.

[28] Gyuhae Park, Hoon Sohn, Charles R Farrar, and Daniel J Inman. Overview of piezoelectric impedance-based health monitoring and path forward. *The Shock and Vibration Digest*, 2003.

[29] Gyuhae Park and Daniel J Inman. Impedance-based structural health monitoring. *Damage prognosis for aerospace, civil and mechanical systems*, pages 275–292, 2005.

[30] Daniel M Peairs, Gyuhae Park, and Daniel J Inman. Improving accessibility of the impedance-based structural health monitoring method. *Journal of Intelligent Material Systems and Structures*, 15(2):129–139, 2004.

[31] Gyuhae Park, Harley H Cudney, and Daniel J Inman. Impedance-based health monitoring of civil structural components. *Journal of infrastructure systems*, 6(4):153–160, 2000.

[32] Gyuhae Park, Harley H Cudney, and Daniel J Inman. Feasibility of using impedance-based damage assessment for pipeline structures. *Earthquake engineering & structural dynamics*, 30(10):1463–1474, 2001.

[33] Mark A Rumsey and Joshua A Paquette. Structural health monitoring of wind turbine blades. In *The 15th International Symposium on: Smart Structures and Materials & Nondestructive Evaluation and Health Monitoring*, pages 69330E–69330E. International Society for Optics and Photonics, 2008.

[34] Niell G Elvin, Nizar Lajnef, and Alex A Elvin. Feasibility of structural monitoring with vibration powered sensors. *Smart materials and structures*, 15(4):977, 2006.

[35] SP Beeby, MJ Tudor, E Koukharenko, NM White, T O'Donnell, C Saha, S Kulkarni, and S Roy. Micromachined silicon generator for harvesting power from vibrations. In *Proceedings of Transducers 2005*, 2004.

[36] Edward Sazonov, Haodong Li, Darrell Curry, and Pragasen Pillay. Self-powered sensors for monitoring of highway bridges. *Sensors Journal, IEEE*, 9(11):1422–1429, 2009.

[37] Peter Glynne-Jones, Michael John Tudor, Stephen Paul Beeby, and Neil M White. An electromagnetic, vibration-powered generator for intelligent sensor systems. *Sensors and Actuators A: Physical*, 110(1):344–349, 2004.

[38] CT Pan and TT Wu. Development of a rotary electromagnetic microgenerator. *Journal of Micromechanics and Microengineering*, 17(1):120, 2007.

[39] Alper Erturk and Daniel J Inman. *Piezoelectric energy harvesting*. John Wiley & Sons, 2011.

[40] Niell Elvin and Alper Erturk. *Advances in energy harvesting methods*. Springer Science & Business Media, 2013.

[41] Henry A Sodano, Gyuhae Park, Donald J Leo, and Daniel J Inman. Electric power harvesting using piezoelectric materials. *Center for Intelligent Material Systems and Structures, Virginia Polytechnic Institute and State University*, 2003.

[42] Dongna Shen, Jung-Hyun Park, Joo Hyon Noh, Song-Yul Choe, Seung-Hyun Kim, Howard C Wikle, and Dong-Joo Kim. Micromachined pzt cantilever based on soi structure for low frequency vibration energy harvesting. *Sensors and actuators A: physical*, 154(1):103–108, 2009.

[43] John Kymissis, Clyde Kendall, Joseph Paradiso, and Neil Gershenfeld. Parasitic power harvesting in shoes. In *Wearable Computers, 1998. Digest of Papers. Second International Symposium on*, pages 132–139. IEEE, 1998.

[44] Loreto Mateu and Francesc Moll. Optimum piezoelectric bending beam structures for energy harvesting using shoe inserts. *Journal of Intelligent Material Systems and Structures*, 16(10):835–845, 2005.

[45] LM Swallow, JK Luo, E Siores, I Patel, and D Dodds. A piezoelectric fibre composite based energy harvesting device for potential wearable applications. *Smart Materials and Structures*, 17(2):025017, 2008.

[46] Youfan Hu, Chen Xu, Yan Zhang, Long Lin, Robert L Snyder, and Zhong Lin Wang. A nanogenerator for energy harvesting from a rotating tire and its application as a self-powered pressure/speed sensor. *Advanced Materials*, 23(35):4068–4071, 2011.

[47] Yong Qin, Xudong Wang, and Zhong Lin Wang. Microfibre–nanowire hybrid structure for energy scavenging. *Nature*, 451(7180):809–813, 2008.

[48] Aneesh Koka, Zhi Zhou, and Henry A Sodano. Vertically aligned batio 3 nanowire arrays for energy harvesting. *Energy & Environmental Science*, 7(1):288–296, 2014.

[49] Hemtej Gullapalli, Venkata SM Vemuru, Ashavani Kumar, Andres Botello-Mendez, Robert Vajtai, Mauricio Terrones, Satish Nagarajaiah, and Pulickel M Ajayan. Flexible piezoelectric zno–paper nanocomposite strain sensor. *Small*, 6(15):1641–1646, 2010.

[50] Yirong Lin, Gregory Ehlert, and Henry A Sodano. Increased interface strength in carbon fiber composites through a zno nanowire interphase. *Advanced functional materials*, 19(16):2654–2660, 2009.

[51] N Masghouni, J Burton, MK Philen, and M Al-Haik. Investigating the energy harvesting capabilities of a hybrid zno nanowires/carbon fiber polymer composite beam. *Nanotechnology*, 26(9):095401, 2015.

[52] Mohammad H Malakooti, Hyun-Sik Hwang, and Henry A Sodano. Power generation from base excitation of a kevlar composite beam with zno nanowires. In *SPIE Smart Structures and Materials+ Nondestructive Evaluation and Health Monitoring*, pages 94320W–94320W. International Society for Optics and Photonics, 2015.

[53] Long Lin, Youfan Hu, Chen Xu, Yan Zhang, Rui Zhang, Xiaonan Wen, and Zhong Lin Wang. Transparent flexible nanogenerator as self-powered sensor for transportation monitoring. *Nano Energy*, 2(1):75–81, 2013.

[54] Tire inspection chart, apr 2016.

[55] Edward F Crawley and Eric H Anderson. Detailed models of piezoceramic actuation of beams. *Journal of Intelligent Material Systems and Structures*, 1(1):4–25, 1990.

[56] C Liang, FP Sun, and CA Rogers. Coupled electro-mechanical analysis of adaptive material systems—determination of the actuator power consumption and system energy transfer. *Journal of Intelligent Material Systems and Structures*, 5(1):12–20, 1994.

[57] Smart Material. Macro fiber composite - mfc, 2016.

[58] Greg Amorese. Lcr/impedance measurement basics. In *1997 Back To Basics Seminar. Hewlett-Packerd. Kobe Instrument Division*. Citeseer, 1997.

[59] X Wang and J Tang. An enhanced piezoelectric impedance approach for damage detection with circuitry integration. *Smart Materials and Structures*, 19(4):045001, 2010.

[60] Jina Kim, Benjamin L Grisso, Jina Kim, Dong Sam Ha, and Daniel J Inman. Electrical modeling of piezoelectric ceramics for analysis and evaluation of sensory systems. In *Sensors Applications Symposium, 2008. SAS 2008. IEEE*, pages 122–127. IET, 2008.

[61] Piezoelectric impedance, apr 2016.

[62] Mohammad I Albakri, Sriram Malladi, and Pablo A Tarazaga. Non-linear impedance-based structural health monitoring for damage detection and identification. In *ASME 2015 Conference on Smart Materials, Adaptive Structures and Intelligent Systems*, pages V002T05A008–V002T05A008. American Society of Mechanical Engineers, 2015.

[63] Lothar Cremer and Manfred Heckl. Structure-borne sound: Structural vibrations and sound radiation at audio frequencies//((book)). *Berlin and New York, Springer-Verlag, 1988, 590*, 1988.

[64] André Preumont. *Mechatronics: dynamics of electromechanical and piezoelectric systems*, volume 136. Springer Science & Business Media, 2006.

[65] Samuel C Stanton, Alper Erturk, Brian P Mann, and Daniel J Inman. Nonlinear piezoelectricity in electroelastic energy harvesters: modeling and experimental identification. *Journal of Applied Physics*, 108(7):074903, 2010.

[66] Liang-zhi Kou, Wan-lin Guo, and Chun Li. Piezoelectricity of zno and its nanostructures. In *Piezoelectricity, Acoustic Waves, and Device Applications, 2008. SPAWDA 2008. Symposium on*, pages 354–359. IEEE, 2008.

[67] Ya Yang, Wen Guo, Xueqiang Wang, Zengze Wang, Junjie Qi, and Yue Zhang. Size dependence of dielectric constant in a single pencil-like zno nanowire. *Nano letters*, 12(4):1919–1922, 2012.